Boundary layer transition induced by low-speed synthetic jets

Andrea Palumbo,[1, a)] Onofrio Semeraro,[2] Jean-Christophe Robinet,[3] and Luigi de Luca[4]

[1)]*Department of Mechanical and Aerospace Engineering, Sapienza University of Rome,*
Via Eudossiana 18, 00184 Rome, Italy

[2)]*LISN, Université de Paris-Saclay, CNRS, 91400 Orsay, France*

[3)]*DynFluid Laboratory, Arts et Métiers ParisTech, 151 Bd. de l'Hopital, 75013 Paris,*
France

[4)]*Department of Industrial Engineering, University of Naples "Federico II",*
80125 Naples, Italy

(Dated: 22 November 2022)

The effect of low-speed, circular synthetic jets (SJ) on the turbulent transition of a laminar boundary layer (BL) is studied through Direct Numerical Simulations (DNS). The SJ capability in fixating the streamwise location of transition onset is analyzed in terms of its operation parameters (reduced frequency F^+ and momentum coefficient C_μ). The effect of free-stream turbulence (FST) on the near-wall vortical structures generated by the synthetic jet is analyzed as well, to mimic the actual operation of the control system. Velocity spectra, phase portraits and dynamic mode decomposition (DMD) allow to investigate flow unsteadiness and transition to a chaotic state. In most of the investigated cases, SJs successfully promote transition, as the result of varicose-symmetric hairpin-like vortices generated at the jet exit. In particular, it is found that increasing the momentum coefficient always reduces the size of the laminar region; a non-monotonic behaviour of the laminar fetch is noted as the reduced frequency is increased, suggesting the existence of an optimal frequency value. Combination of FST and SJ actuation results in spanwise-asymmetric vortical structures, with little difference in the location of the transition onset as compared to the previous case. The present analysis can be used to gather information on the practical implementation of low-speed SJ actuators as active turbulators.

a)Electronic mail: andrea.palumbo@uniroma1.it

I. INTRODUCTION

Optimizing the aerodynamic performance of aircraft is one of the key goals of the fluid-dynamic community. The research on this topic suggests that flow separation can be largely responsible for efficiency losses on lifting surfaces. Several flow control strategies have been therefore proposed during the last decades to delay or, if possible, suppress flow separation. For low-speed flows, a common strategy aims at triggering turbulent transition sufficiently upstream of uncontrolled detachment, as turbulent boundary layers are more resistant to separation than a laminar one. In this context, transition-promoting devices are generally referred to as turbulators[1].

A large number of fluid systems has been proposed at this aim[2], including roughness elements[3] and micro vortex generators[4]. However, any flow control system able to introduce large disturbances into the boundary layer, hence causing its bypass transition, can be used as turbulator. In this respect, synthetic jet (SJ) actuators have already demonstrated their potential thanks to their flexibility, reduced sizes and weights and relatively low energy consumption. Although different technologies can be used to obtain synthetic jets, most studies employed piezo-driven actuators[5]. These actuators are capable of generating controlled vortex motion from periodic volume oscillations of a resonant cavity, which are driven by vibrations of a piezo-element located at its bottom end. The topology of the flow structures injected into the external environment by the synthetic jet ranges from hairpin-like vortices, for relatively small momentum injection, to vortex rings of different shape, depending on the SJ operation parameters and geometry[6–8].

The state of the vortical structures issued by a synthetic jet into a quiescent environment can be exhaustively defined by means of two non-dimensional parameters, the Stokes number (S) and the jet Reynolds number (Re_j). Among other things, these parameters control jet formation[9], vortex trajectory and spacing[5]. In a similar way, the interaction between a synthetic jet and a crossflow is generally characterized in terms of two parameters. The momentum coefficient C_μ is defined as the ratio between the jet and the crossflow momentum fluxes, whereas the reduced frequency F_j^+ is the ratio between the actuation frequency and an intrinsic frequency of the uncontrolled flow.

Whereas several research activities have dealt with industrial and commercial applications, in which the synthetic jet is used to control separation on bluff bodies[10,11], lifting surfaces[12–14] or ramp-like geometries[15,16], other works have been focused specifically on the underlying flow mechanism determining its control effectiveness. The latter studies mainly regarded the interaction between a synthetic jet and a zero-pressure gradient boundary layer. A notable feature, resulting

from these analyses, is the *virtual aeroshaping effect*[17,18]: if the actuator is driven at very high reduced frequency and momentum ratio, large time-averaged separation bubbles can be generated. This effect can be used to obtain large modifications to the uncontrolled flow with limited energy expenditure[15].

Other works analyzed the flow topology of the structures generated by the interaction between the jet and the boundary layer. Jabbal and Zhong[19] and Zhou and Zhong[6] considered a laminar, low-Reynolds-number case, visualized the main coherent structures in the near-field region and investigate their effect in terms of wall shear stress. They identified three main flow regimes: for low values of the momentum coefficient the flow features near-wall hairpin vortices, whereas circular or distorted vortex rings are created for higher values, depending on the actuation frequency. Similar findings have been obtained more recently for plasma synthetic jets[20] and slotted actuators[7,21].

It is nowadays well known that hairpin-like structures can be generated by the jet/laminar boundary layer interaction[6,19]; these structures can be responsible for early transition (with respect to the uncontrolled case), near-wall mixing enhancement and skin-friction coefficient increase in the streamwise direction. However, most studies are restricted to completely laminar or completely turbulent crossflows, whereas minor attention has been paid to the transitional case. To the authors' knowledge, the only studies involving transitional flows of synthetic jet in crossflow are the ones by Wang and Feng[21], Van Buren *et al.*[7] and Xiao *et al.*[22]. The former two studies employed a slotted synthetic jet to analyze the effect of slot orientation with respect to the cross-flow, whereas the latter considered the bypass transition due to dielectric barrier discharge (DBD) actuators. Very little information on the typical streamwise and spanwise lengthscales associated with boundary layer transition due to circular synthetic jet can be gathered from literature at the present state.

The present work presents numerical results about the transition of a laminar boundary layer induced by synthetic jets. Specifically, the main goal is to conduct a parametric analysis on the effect of synthetic jet's operation parameters on its effectiveness as a transition-promoting device. In addition, the effect of FST on the control efficiency is examined, to investigate its robustness to inevitable in-flight and wind tunnel disturbances. It is noteworthy that the DNS approach followed in the present work allows to quantitatively estimate the effect of synthetic jet actuation on the development of both the disturbances and the boundary layer properties along streamwise and spanwise directions. In addition, these distributions are examined either in case of a perfectly

3

laminar inflow condition or in presence of freestream turbulence. The use of three-dimensional data would be crucial for the design of a synthetic jet array able to get a turbulent flow state, covering the entire spanwise extent of the bounding surface, at a certain streamwise location.

Another innovative aspect of the work with respect to previous literature is that the analysis focuses on SJ actuation for low values of C_μ and $F_j^+ = \mathcal{O}(1)$, in which Tollmien-Schlichting waves are considered as a reference frequency scale. This low-C_μ/low-frequency framework would be more energy-efficient than virtual aeroshaping, which certainly needs higher operation frequency. It is worth noting that the term 'low-speed' SJs herein used does refer to the fact that the jet blowing ratio is smaller than in typical flow control studies, as will be discussed in section II. In fact, the perturbation energy imparted by the SJ actuator in the present work are order of magnitudes larger than the one applied for TS-wave work, and this will lead to bypass transition. The TS wave frequency is therefore used as a mere frequency scale, as TS waves are not expected to play any role in the non-linear transition process obtained with the present flow control setup.

Low-speed SJs would be also more suited for practical applications than passive vortex generators, which can introduce strong wake drag in off-project conditions. One of the main advantages of active fluid-based devices (such as SJ actuators) is their possibility of being flexible means of flow control, which can adapt dynamically to the crossflow conditions. In addition, SJs actuators can be turned off when their control is not required, with minimal performance loss (the nozzle exit can be also automatically obstructed by gates in inoperative conditions to minimize the hole interference). These two features cannot be obtained - at least not together - neither by passive controls, nor by conventional piping, which requires on-board plumbing systems, thus increasing the overall size and weight of the device. Providing design guidelines for low-speed synthetic jets in crossflow would be a valuable result, which will pave the way to their application as 'green technologies' to trigger transition to turbulence. Finally, mapping the $C_\mu - F^+$ space in terms of control authority of the jet constitutes a mandatory step for the development of more complex control devices, possibly involving active learning techniques[23].

The structure of the present paper is outlined in the following: the computational setup is described in section II. The results of one of the numerical simulations included within the numerical campaign (which will referred to as "reference" in the following) are outlined in section III. The results of the parametric analysis, in terms of the actuation reduced frequency and momentum coefficient, are discussed in section IV, along with the investigation of the combined effect of SJ actuation and FST. A spectral analysis of the vortical structures generated by the interaction be-

4

tween the jets and the boundary layer is presented in section V. Finally, conclusions are drawn in section VI.

II. NUMERICAL SETUP AND FLOW CONFIGURATION

High-fidelity, direct numerical simulations of the synthetic jet in crossflow are carried out by means of the open-source code Nek5000 (nek5000.mcs.anl.gov). The choice of Nek5000 is guided by recent literature works, where it has been employed for the simulation of synthetic jets in quiescent conditions[24] and controlled transition of boundary layer via miniaturized roughness elements[25]. The spectral element method applied in the present work is based on the $\mathscr{P}_N - \mathscr{P}_{N-2}$ formulation, meaning that the velocity field is discretized onto N-th degree Lagrange interpolants, whereas the pressure field is discretized using Lagrange interpolants of degree $N - 2$. The N-th and $N - 2$-th degree polynomials are based, respectively, on the Gauss–Lobatto-Legendre quadrature points and the Gauss–Legendre ones. After a preliminary grid convergence study, the polynomial degree is fixed to $N = 9$ for the present numerical campaign, whereas the mesh is composed of about 30000 hexahedral elements; the assessment of the quality of the present numerical setup, in terms of grid and domain dependence analysis and effect of jet inflow condition, is discussed in Appendix A.

The computational domain is sketched in figure 1. It is composed of a parallelepiped region of dimensions L_x, L_y and L_z (where x, y and z axes run along the streamwise, the wall-normal and the spanwise crossflow directions, and the reference system is centered on the geometric center of jet exit section), and a cylindrical pipe, of height H and diameter D. The domain dimensions are chosen as $L_x = 55D$, $L_y = 10D$, $L_z = 10D$ and $H = 5D$, and the jet is injected perpendicularly to the crossflow direction by means of a flush nozzle. Both continuous and synthetic jets are simulated, subjected to the same boundary layer inflow conditions. Nonetheless, the continuous jet in crossflow simulations will be not the object of the present study, as they were used mainly for validation purposes.

The choice of the pipe length H/D is made according to preliminary computations (discussed in appendix A), which reveal that for $H/D \geq 5$ no significant differences are observed on the resulting flow field. It is worth remarking that the inclusion of the inlet pipe within the three-dimensional computations of the jet in crossflow is crucial to properly model the flow, as the crossflow strongly affects the characteristics of the jet underneath its exit section. A Dirichlet condition is enforced at
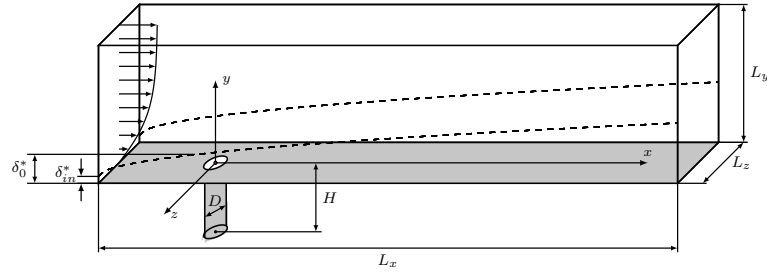
5

FIG. 1. Sketch of the computational setup and domain dimensions. No-slip conditions are applied on gray patches. The streamwise development of the unforced boundary layer (not to scale) is reported as a thin dashed line.

the bottom end of the inlet pipe, $y = -H$: it is obtained from the analytical (Womersley) solution of a fully-developed pulsating laminar pipe flow, given as

$$\frac{v(r,t)}{U_\infty} = R^* \cdot \text{Real} \left\{ \left[1 - \frac{J_0(i^{3/2} Wo\, r)}{J_0(i^{3/2} Wo)} \right] e^{i\omega_j t} \right\}, \qquad y = H \tag{1}$$

where $V = (u, v, w)$ is the instantaneous flow velocity, $\omega_j = 2\pi f_j$ is the circular actuation frequency, J_0 is 0-th order Bessel function, $r = \sqrt{2/D(x^2 + y^2)}$ the axial distance from the pipe symmetry axis (made dimensionless against the pipe radius), $Wo = \sqrt{\omega_j D^2/4\nu}$ the Womersley number and $R^* = V_j/U_\infty$ is the velocity ratio between the jet and the crossflow, defined in terms of the centerline velocity at ejection peak V_j. Further information on this boundary condition are given in appendix B. The boundary layer inflow is located $10D$ upstream of the nozzle axis. Homogeneous Dirichlet conditions are applied at all the solid walls (depicted in gray in figure 1), whereas a Blasius velocity profile is applied at the inlet section. In particular, the value of the displacement thickness of the uncontrolled flow δ_0^* at the nozzle axis is initially assigned, and the boundary layer thickness δ_{in}^* is retrieved using the Blasius similarity law.

A mixed Dirichlet/Neumann boundary condition ($u = U_\infty$, $v_y = 0$, $w_y = 0$, where the subscripts denote partial differentiation) is applied on the top of the domain $y = L_y$, whereas a natural outflow condition $-pn + \nu \nabla U \cdot n = 0$ is enforced at the streamwise outlet boundary $x = x_{max}$ (involving the instantaneous reduced pressure p and the kinematic viscosity ν, whereas n is the outward-pointing normal vector to the outlet surface). The generation of the boundary layer inflow is

6

discussed in section II A, with a special focus to the FST case. Pressure boundary conditions are automatically enforced by the Nek5000 code to ensure incompressibility. Finally, periodic boundary conditions are applied on the spanwise ends of the domain: preliminary studies have been made to demonstrate that the numerical results are not influenced by the spanwise width of the domain. The results of the domain dependence analysis are shown in appendix A.

The initial condition for all simulations is a spatially-developing Blasius boundary layer for the external domain, whereas the pipe is initially in quiescent conditions. Time integration is performed by means of a high-order splitting method (BDF3-EXT3)[26,27], in which a third-order extrapolation is used for the convective terms (EXT3), while the viscous terms are discretized implicitly with a third-order backward discretization scheme (BDF3). The same time-step is used for all simulations, corresponding to a constant Courant number of about $C = 0.5$, leading to about 20000 time-steps per actuation cycle. All the simulations are carried out in two steps: an initial subset of the simulation is used to remove transient effects, while time-averaged quantities and velocity spectra are collected during the last ten cycles. Preliminary computations obtained by doubling the number of averaging cycles revealed that both time-averaged results and velocity spectra are well converged if ten accumulation cycles are used.

A. FST modelling

The inflow condition is chosen to mimic the features of an actual boundary layer profile interacting with the SJ in both wind tunnel experiments and in-flight conditions. The inflow condition is obtained as the superposition of a standard Blasius profile with synthetic turbulence, as shown in the paper by Brandt *et al.*[28]: FST frequencies and amplitudes are chosen from Von Karman's homogeneous-isotropic turbulence spectrum,

$$E(k) = \frac{1.606(kL)^4}{(1.350 + (kL)^2)^{17/6}} L Tu_\infty^2.$$ (2)

whereas the FST shape is obtained as a combination of a subset of Orr-Sommerfeld/Squire (OSS) modes. In equation (2) L is the integral length scale of the turbulence, k the wavenumber, and

$$Tu_\infty = \frac{1}{U_\infty} \sqrt{\frac{u_{\mathrm{rms},\infty}^2 + v_{\mathrm{rms},\infty}^2 + w_{\mathrm{rms},\infty}^2}{3}}$$

the freestream turbulence intensity (where $u_{\mathrm{rms},\infty}, v_{\mathrm{rms},\infty}, w_{\mathrm{rms},\infty}$ are the freestream values of the velocity fluctuations). The implementation of the FST modelling in Nek5000 used in the present
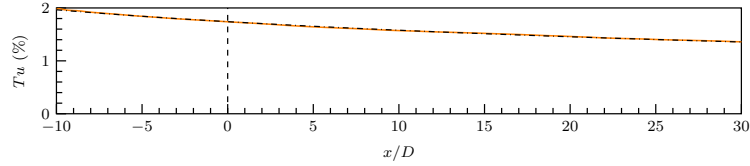
FIG. 2. Time- and spanwise-averaged turbulent intensity distribution Tu along the streamwise direction (orange solid line) and the analytical law $Tu \propto (x-x_0)^{-0.5}$ (black dash-dotted line). A vertical dashed line indicates the position of the jet axis. Case S9 of table I, $y = 20\delta_0^*$.

work is presented in Bucci *et al.*'s work[29], and the code validation was performed against the very same test case of Brandt *et al.*[28]. A value of $L = 5\delta_0^*$ is chosen for all the simulations, as in one of the computational cases of Brandt *et al.*[28]; such a value of the integral length is also fairly consistent with the numerical results of Jacobs and Durbin[30], whose low-turbulence simulation reaches comparable values of L and Tu at the streamwise location where $Re_{\delta^*} = U_\infty \delta^* / \nu = 500$.

The streamwise distribution of the freestream time-averaged turbulence intensity at $y = 20\delta_0^*$ is shown in figure 2, for the case S9 described in table I ($Re_{\delta_0^*} = U_\infty \delta_0^* / \nu = 550$, $Tu_\infty = 2\%$). One can observe that the turbulent intensity decreases monotonically from the inlet boundary in agreement with the aforementioned study, following the scaling law $Tu \propto (x-x_0)^{-n}$, where x_0 is the virtual origin of the boundary layer (i.e. the streamwise distance from the leading edge of the flat plate which is required, according to Blasius theory, to obtained the fixed value of δ_{99} at the jet exit); the constant n is found to be equal to 0.5 for the considered cases, in accordance with the wind tunnel experiments by Shahinfar[31] and Fransson and Shahinfar[32].

B. Non-dimensional parameters and computational cases

The synthetic jet characteristics are generally described by means of jet Reynolds number $Re_0 = V_0 D/\nu$, Strouhal number $St_0 = \omega_j D/V_0$ and Stokes number $S = \sqrt{\omega_j D^2/\nu} = 2Wo$, where V_0 is the averaged jet blowing velocity defined as

$$V_0 = \frac{1}{A_j}\frac{1}{T}\int_0^{T/2}\left[\iint_{A_j} V(x,y=0,z)dxdz\right]dt, \tag{3}$$

$T = 1/f_j$ the actuation period, $A_j = \pi D^2/4$ the jet exit area, and Wo the Womersley number, introduced before. Such a velocity scale has been originally conceived by Smith and Glezer[33] for

8

a slotted SJ in quiescent conditions, and recently employed in several research activities involving synthetic jets in crossflow[7,34]. For high Stokes numbers, the averaged jet blowing velocity is linked to the previously introduced peak centerline velocity V_j as $V_0 = V_j/\pi$. Another widespread definition of the reference velocity is the momentum one, originally defined by Cater and Soria[35], which can be obtained from the previously defined one as $V_0 \pi / \sqrt{2}$. It is worth noting that only two of the three dimensionless quantities defined above can be chosen independently, as the relation $St_0 = S^2/Re_0$ between the aforementioned parameters holds.

As anticipated in section I, the interaction between the synthetic jet and boundary layer needs to be described by further quantities. The ratio between the unforced boundary layer displacement thickness δ_0^* at the nozzle axis streamwise location and the jet diameter D is used to define the (virtual) position of the actuator; this dimensionless quantity is fixed to $\delta_0^*/D = 0.25$ for all simulations. Moreover, the strength and the actuation frequency of the jet are quantified through the momentum coefficient and the reduced frequency, defined as

$$C_\mu = \frac{\rho_j V_0^2}{\rho_\infty U_\infty^2} \frac{D}{\theta_0}, \qquad F_j^+ = \frac{f_j}{f_{ref}}, \qquad (4)$$

where the actuation frequency f_j is scaled with the frequency (f_{ref}) of the most spatially amplified Tollmien-Schlichting (TS) wave, and θ_0 is the uncontrolled momentum thickness at the jet streamwise location. The value of the reference frequency is obtained by means of spatial, linear stability analysis at the streamwise location of the nozzle centerline (when the jet is off), carried out using a dedicated eigenvalue solver for the linearized Navier-Stokes operator. For $Re_{\delta_0^*} = 550$, $f_{ref}D/U_\infty = 0.0752$ is obtained (corresponding to a period of about 13.3 time units). The momentum coefficient C_μ is obtained as the ratio between the jet momentum flux and the one of the boundary layer fetch interested by SJ actuation. It is assumed that the reference momentum flux of the airflow interacting with the jet is proportional to $\theta_0 D$[18]. It is noteworthy that, in the present study, variations in the momentum coefficient are only possible due to different V_0 values, as all the other parameters are kept unchanged within the computational campaign.

The numerical simulations performed in the present work are summarized in table I. The effect of changes in the reduced frequency, the momentum coefficient and the receptivity to FST are thoroughly investigated. For all simulations the crossflow Reynolds number is chosen as $Re_{\delta_0^*} = 550$, corresponding to a local Reynolds number $Re_{x_0} = U_\infty x_0/\nu \approx 10^5$.

First of all, simulations S2-S6 are carried out to analyze the transitional behaviour of the flow for different values of the reduced frequency. Simulations are performed at $F_j^+ = \{0.5, 2, 2.5, 3.125, 4\}$:

9

Case	BL parameters				SJ parameters				Line style
	$Re_{\delta_0^*}$	δ_0^*/D	$Tu_\infty(\%)$	R^*	Re_0	S	C_μ	F_j^+	
S1	550	0.25	–	0.1	70	32.2	0.0105	1.00	▬
S2	550	0.25	–	0.1	70	22.8	0.0105	0.50	▬
S3	550	0.25	–	0.1	70	45.6	0.0105	2.00	▬
S4	550	0.25	–	0.1	70	50.9	0.0105	2.50	▬
S5	550	0.25	–	0.1	70	56.9	0.0105	3.125	▬
S6	550	0.25	–	0.1	70	64.4	0.0105	4.00	▬
S7	550	0.25	–	0.05	35	32.2	0.0026	1.00	▬
S8	550	0.25	–	0.075	52.5	32.2	0.0059	1.00	▬
S9	550	0.25	2.0	0.1	70	32.2	0.0105	1.00	▬
S10	550	0.25	4.0	0.1	70	32.2	0.0105	1.00	▬

TABLE I. Summary of the computational cases.

the investigated frequency range covers both the frequency of two- and three-dimensional Tollmien-Schlichting waves and the reference frequency for the corresponding jets in crossflow (which, not shown herein, is characterized by the advection of hairpin-like vortices at $F^+ = f/f_{ref} \approx 3$).

As regards the momentum coefficient analysis, it is chosen small enough to operate in a very low-consumption regime. Three different values of the momentum coefficient are analyzed: C_μ=0.0105 (for the most part of the simulation campaign), C_μ=0.0026 for case S7, C_μ=0.0059 for case S8, corresponding to velocity ratios of R^*={0.1, 0.05, 0.075}, respectively. An alternative definition of the velocity ratio can employ the blowing ratio[8] $C_B = V_0/U_\infty \approx V_j/(\pi U_\infty)$. In the present cases, values of the blowing ratio range between 0.016 and 0.032, much lower than the typical values used in flow control applications[17,36].

Finally, the inlet freestream turbulent intensity is fixed to 0 for S1-S8 simulations; S9 and S10 cases are devoted to investigating the effect of Tu_∞ on the reference case, by imposing, respectively, Tu_∞=0.02 and Tu_∞=0.04. Similar values of free-stream turbulence intensity were previously investigated by other research groups[28,30,31], both by experiments and numerical simulations, and clearly exceed the typical ones observed on aircraft. However, preliminary studies at smaller turbulence levels, $Tu_\infty \leq 1\%$, (not shown herein) demonstrate that the vortical structures

induced by the actuator are basically unaffected by FST at those conditions. The extremely high FST intensity investigated herein is used to provide a sort of 'stress test' for the actuator, in which FST is able to play a role into the turbulent development of the flow. Besides, It must be highlighted that the inflow BL properties for the reference case match the previous studies of Jabbal and Zhong[19] and Zhou and Zhong[6] in terms of $Re_{\delta_0^*}$ and St_0, which however involve a much higher value of δ_0^*/D, a shorter orifice and higher velocity ratios. For this reason, the results of the present numerical campaign are not directly comparable with their experimental/numerical findings.

III.   REFERENCE CASE

The distinctive features of the interaction between synthetic jet and laminar boundary layer are documented in the present section, with reference to the S1 case ($C_\mu = 0.0105$, $F_j^+ = 1$, $Tu_\infty = 0$). The aim of this section is two-fold: first, characterize the turbulent development of the flow, detecting the main vortical structures generated at the jet exit, the modification of the mean flow and the unsteadiness induced by the control actuation. Second, the present section is also intended to introduce the main diagnostic quantities that will be used in the subsequent parametric analyses. It is worth remarking that the present analysis is focused on monitoring the onset of transition and the spanwise extent of the turbulent region generated by the control system. Further information on instantaneous and time-averaged flow topology can be found in literature, as reviewed by Mohseni and Mittal's textbook[36].

A.   Instantaneous flow field

Figure 3 depicts the evolution and the transition to turbulence of the vortical structures generated by the interaction of the synthetic jet with the incoming crossflow, at the end of the last actuation cycle. Their visualization is obtained by using isosurfaces of the λ_2 criterion[37]. It must be remarked that only a small subset of the domain is shown in figure 3 (and in the following ones). In fact, the actual transverse dimension of the computational domain is $L_z = 10D$, whereas the following figures are focused on $-2.5 \leq z/d \leq 2.5$ only.

As observed in the numerical simulation by Zhou and Zhong[6] for a low-Re and low-C_μ case, the near field is dominated by the presence of hairpin vortices, which move downstream of the orifice at an initially constant speed. It is worth noting that, due to the relatively low strength of
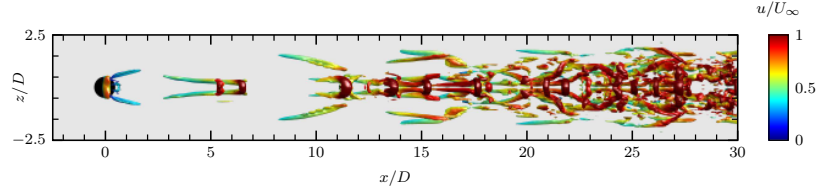
11

FIG. 3. Streamwise evolution of the vortical structures arising from the jet-boundary layer interaction: isosurfaces of $\lambda_2 = -0.025$ coloured by values of the instantaneous streamwise velocity component. Case S1, $t/T = 10$.

the control actuation, no horseshoe vortex is detected upstream of the nozzle.

The downstream evolution of the hairpin structures is characterized by a sudden reduction of their convection speed, leading to their merging and interaction. The convection velocity U_c of the vortices at a reference location $(x/D, y/D, z/D)$ is obtained by plotting the spatio-temporal correlation of the streamwise velocity fluctuation from the time-averaged flow $\overline{u}$, namely $u_f = u - \overline{u}$, defined as

$$R_{uu}(x,t;r,\Delta t) = \frac{\overline{u_f(x,t)u_f(x+s,t+\Delta t)}}{\sqrt{\overline{u_f^2(x,t)}}\sqrt{\overline{u_f^2(x+s,t+\Delta t)}}} \tag{5}$$

and evaluating it as $U_c = s_{max}/\Delta t$, where s_{max} is the streamwise distance for which the correlation is maximum at a given Δt[38]. In particular, the convection velocity is obtained by monitoring the distance covered by the vortices during the first half of the actuator cycle (corresponding to the minimum value of R_{uu} along the horizontal line $\Delta t/T = 0.5$ in figure 4(a)), and dividing it for the corresponding time scale.

Figure 4(a) depicts a contour plot of the spatio-temporal correlation R_{uu} at $(x/D, y/D, z/D) = (5, 0.125, 0)$: the convection velocity at this point is $\approx 0.45U_\infty$, corresponding to a streamwise wavelength of about $6D$. Such a result is found to be independent from the choice of the wall-normal coordinate (if the reference point falls within the boundary layer). Figure 4(b) shows the U_c distribution along the streamwise direction: it is initially constant ($U_c = 0.45U_\infty$), then sharply drops to smaller values and increases again at the start of the transition region. The value of U_c in the near field is comparable to the velocity of the Tollmien-Schlichting wave obtained for a frequency equal to the actuation one ($U_c = 0.39U_\infty$, red line in figure 4(b)). Its following increase is justified by the modification of the streamwise velocity profile in the transition region, which is

12
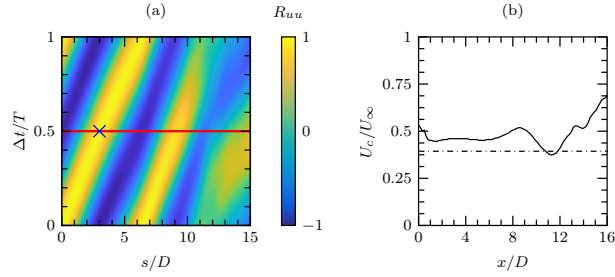
FIG. 4. (a) Contour map of the spatio-temporal correlation of the streamwise velocity fluctuations R_{uu}, at $(x/D, y/D, z/D) = (5, 0.125, 0)$. A horizontal red line represents $\Delta t/T = 0.5$; a blue cross denotes the peak position of R_{uu} on this line. (b) Convection velocity (black line) U_c as a function of the streamwise direction x/D, for a fixed wall-normal height $y/D = 0.125$ and corresponding TS-wave velocity (black dashed-dotted line). Case S1.

characterized by a flatter shape than the Blasius one, as shown in Section III C.

As a general result, it can be noted that the flow field becomes very complicated, being characterized by the interaction between adjacent vortices, spreading and break-up. However, it is apparent that even in the far field the instantaneous flow field is characterized by a varicose-symmetric structure, meaning that a sustained turbulent state is not reached at the end of the domain. This feature is demonstrated by the time evolution of the velocity in selected probes (figure 5, left panel), located at increasing distances from the jet exit plane: the velocity field maintains a deterministic behaviour. This feature is confirmed by the phase portraits in figure 5, right panel, which represent the result of the time-delay embedding technique[39,40], applied to the velocity time series with temporal delay $\tau = 1/(4f_j)$. One can note that after the transient phase (not included in the phase trajectories), the system follows a limit-cycle behaviour, which is more complicated in the far-field region due to the growing importance of high-frequency fluctuations.

The modification induced by the hairpin vortices on the mean flow can be appreciated by analyzing the instantaneous velocity field at different streamwise stations. Figure 6 shows the instantaneous streamwise velocity deviation from the Blasius solution. It can be observed that the effect of the vortices is to induce, in the near field, an upwash of the fluid next to the symmetry plane and a downwash in the external region. In other words, the hairpin vortices generated by the interaction of the pulsed jet with the crossflow are able to entrain fluid efficiently in the near

13
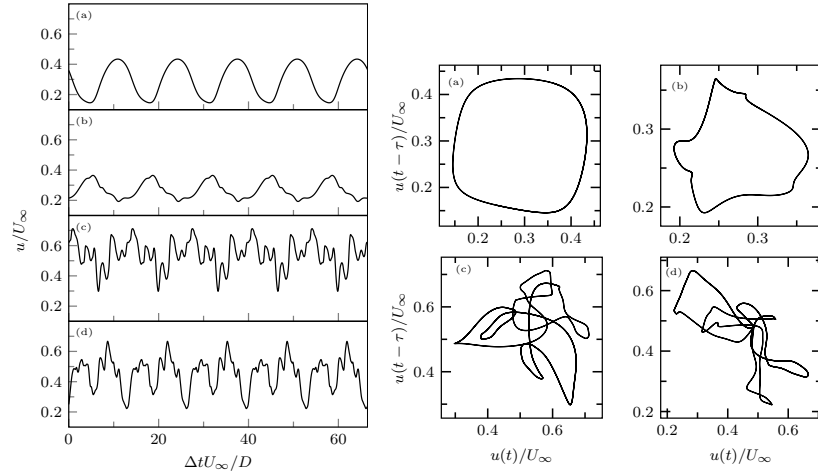
FIG. 5. (left) Time variation of the streamwise velocity component during the last 5 actuation cycles, at different streamwise positions in the symmetry plane $(x/D, y/D)$: (a) $(0, 0.125)$,(b) $(10, 0.125)$,(c) $(20, 0.125)$,(d) $(30, 0.125)$; (right) Phase portraits of the same velocity signals. Case S1.

wall region and to induce a fluid uplift in the central one. In the downstream region the vortical structures generated in the near field depart from the wall, while new vortices are created in the wall region. In the far field the original hairpin vortices are far enough from the plate to organize themselves in an annular shape, while several small structures appear within the boundary layer region. The overall effect on the streamwise velocity component consists of an increase (growing with x) next to the wall, and a reduction in the core of the main vortex.

The lateral spreading of the hairpin structures can be qualitatively investigated by means of the spanwise distribution of the time-averaged streamwise velocity deviation from the Blasius solution (shown in figure 6) or more quantitatively by inspecting the velocity root mean square $u_{\mathrm{rms}}/U_\infty$ within a given wall-normal plane. The latter flow feature is depicted in figure 7: the spanwise extent of the region of non-negligible velocity fluctuation is initially bounded by the jet exit dimensions and subsequently spreads with an approximately constant growth rate (for $x/D \geq 12$). The half-spreading angle for $12 \leq x/D \leq 30$ is $\approx 5°$, reaching about $l_z \approx 1.8D$ for $x/D = 30$; such a parameter has been obtained by assuming a constant contour value of $u_{\mathrm{rms}}/U_\infty = \sqrt{\overline{u_f u_f}}/U_\infty = 0.11$ as a proxy for identifying the spanwise region covered by the hairpin vortices.

14
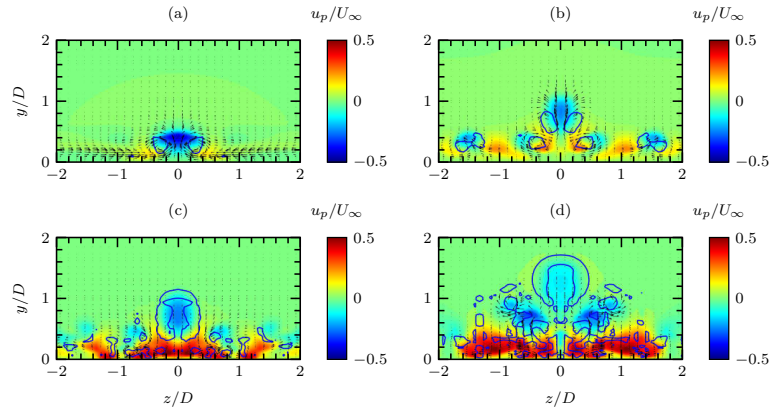
FIG. 6. Contour plot: instantaneous streamwise velocity deviation component $u_p = u - u_{Bl}$ at different streamwise stations; blue lines: isolines of $\lambda_2 = -0.025$ for vortex visualization; black vectors: instantaneous in-plane velocity. (a) $x/D = 5$; (b) $x/D = 15$; (c) $x/D = 25$; (d) $x/D = 30$. Case S1, $t/T = 10$.
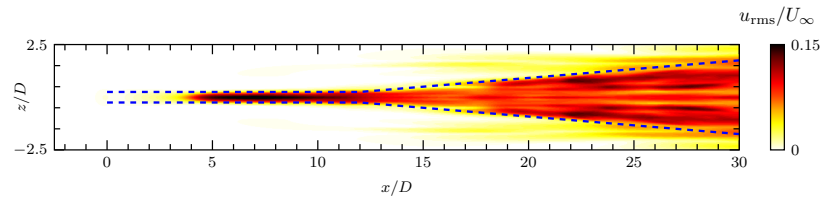

FIG. 7. Contour plot of the time-averaged velocity fluctuation $u_{\mathrm{rms}}/U_\infty$ in a plane parallel to the $x - z$ plane, $y/\delta_0^* = 2$, with indication of the hairpin width (blue dashed lines, $u_{\mathrm{rms}}/U_\infty = 0.11$). Case S1.

A similar procedure has been carried out by Ye et al.[41] for the analysis of the transitional flow behind a micro-ramp, leading to a spreading rate value in good agreement with the present results.

Lastly, it is worth noting that the instantaneous flow field is qualitatively similar to the turbulent flow behind an isolated roughness element, which is the result of the breakdown of the streaky structures originated downstream of the element. The reader can compare, for instance, figure 3 with a major result of the numerical campaign carried out by Bucci et al.[25] for similar crossflow conditions (figure 18, page 185 of the cited paper): while stable streaks are able to delay turbulence by affecting the growth of the TS unstable mode, in supercritical cases the streaks become unsta-

15

ble themselves, leading to early transition. The vortical structures downstream of the roughness element resemble the ones shown in figure 3.

B.   Streak amplitude and fluctuations

The departure from the laminar solution and the strength of the hairpin structures generated at the jet exit section can be investigated by defining a proper index for the velocity deviation imparted by SJ actuation. Following Siconolfi et al.'s definition[42], this quantity is measured as the integral of the difference between the local streamwise velocity and the spanwise-averaged one $u^z(x,y)$

$$A_{st}^{int}(x) = \frac{1}{U_\infty} \int_{-1/2}^{1/2} \int_0^{\eta^*} |\bar{u}(x,\eta,\bar{z}) - u^z(x,\eta)| \, d\eta \, d\bar{z}, \tag{6}$$

where the wall-normal coordinate $\eta = y/\delta(x)$ is made non-dimensional against the local boundary layer conventional thickness of the uncontrolled flow and $\bar{z} = z/L_z$. The value of η^* is chosen large enough to obtain that the integral in equation (6) is independent of its value for all the simulations; in the present study $\eta^* = 5$ is fixed. To better understand the significance of the newly introduced quantity, figure 8(a) shows the distribution of the local velocity deviation, integrated in the wall-normal direction only

$$\bar{u}_{d,y}(x,z) = \frac{1}{U_\infty} \int_0^{\eta^*} [\bar{u}(x,\eta,\bar{z}) - u^z(x,\eta)] \, d\eta, \tag{7}$$

Comparing it with the instantaneous flow field in figure 6 it can be inferred that the time-averaged flow field is characterized by the presence of two pairs of streamwise streaks located in the vicinity of the wall. These streaks clearly fade away from the symmetry plane in this near-field, and their amplitude increases while moving downstream. The far field is instead dominated by the presence of several elongated streamwise structures, which are the result of the near-wall instantaneous turbulent motion depicted in figure 6. As a whole, the amplitude of the streaks is monotonically increasing along the entire streamwise extension of the domain, and its growth rate sharply rises at the beginning of the transition region.

As the integrated streak amplitude can exhaustively explain the mean-flow perturbation induced by the synthetic jet, another quantity is introduced to investigate the flow unsteadiness. The integrated fluctuating energy $K_{int}(x)$, originally defined by Van Buren *et al.*[7], is used at this purpose. It is defined as follows

$$K_{int}(x) = \frac{L_z}{2U_\infty^2 D^2} \int_{-1/2}^{1/2} \int_0^{L_y} (u_{\text{rms}}^2 + v_{\text{rms}}^2 + w_{\text{rms}}^2) \, dy \, d\bar{z}, \tag{8}$$
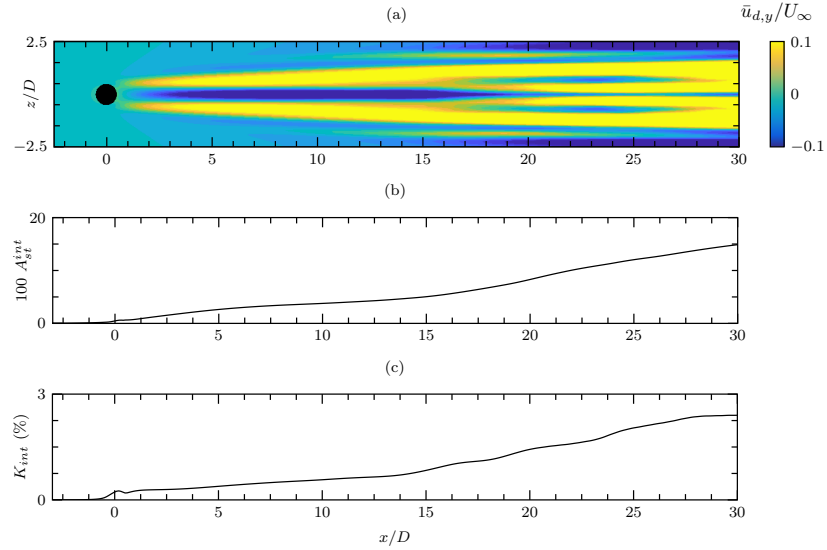
16

FIG. 8. Contour plot of the integrated velocity perturbation $\overline{u}_{d,y}$ (a), streamwise distribution of streak amplitude A_{st}^{int} (b) and integrated fluctuation energy K_{int} (c). Case S1.

As noted by Van Buren[7], this quantity accounts both for coherent unsteadiness generated by the jet and actual turbulent fluctuations. The above defined quantity is reported in Fig. 8 (c), which shows a monotonic increase of K_{int} along the streamwise direction, ultimately reaching a value of $\approx 2.4\%$ at the end of the domain fetch under scrutiny.

C. Time-average integral parameters

Finally, time-averaged flow quantities can be an effective tool to investigate the capability of the synthetic jet actuator in anticipating the transition onset and hence modifying the boundary layer streamwise development. This goal can be achieved by inspecting the streamwise distribution of the time-average skin friction coefficient $C_f = 2\overline{\tau}_w/(\rho U_\infty^2)$ (where $\tau_w = \mu u_y(y=0)$ is the local

17

wall shear stress) and shape factor H, defined as

$$H(x) = \frac{\delta^*(x,z)}{\theta(x,z)} = \frac{\int_0^\infty 1 - \frac{\overline{u}(x,y,z)}{U_\infty} dy}{\int_0^\infty \frac{\overline{u}(x,y,z)}{U_\infty}\left(1 - \frac{\overline{u}(x,y,z)}{U_\infty}\right) dy}, \tag{9}$$

where δ^* and θ are the boundary layer displacement and momentum thicknesses. The departure from a laminar solution can be studied by comparing the controlled flow distributions both with laminar boundary layers, provided by Blasius theory[43], whose results are summarized as follows

$$C_{f,lam} = \frac{0.664}{\sqrt{Re_x}}, \qquad H = 2.59, \tag{10}$$

and the turbulent correlation law by White[43]:

$$C_{f,turb} = \frac{0.455}{\log^2(0.06Re_x)}. \tag{11}$$

Figure 9 depicts the distribution of the above defined quantities along the symmetry plane $z = 0$ (top panel) and several wall-normal distributions of time-average streamwise velocity along the symmetry axis (bottom panel). Both boundary layer parameters sharply depart from the laminar solution just downstream of the jet exit section, with a sudden drop of the shape factor H and a corresponding C_f increase. Increasing trends of friction coefficient and momentum thickness are justified by the velocity profiles, which present high near-wall velocity in the controlled case. The scenario outlined in figure 9 is consistent with the results of the spatio-temporal correlation analysis. The convection velocity of the hairpin-like structures generated by the synthetic jet increases in the transitional region because of the higher momentum in the near-wall part of the boundary layer. In this respect, a relation between the distribution of the skin friction coefficient C_f and the convection velocity is apparent. The smallest convection velocity occurs where the C_f is minimized and increases accordingly in the subsequent region.

The evolution of the shape factor H reveals that this parameter immediately reduces from the laminar value, eventually attaining the value of $H \approx 1.5 - 1.6$, which are typical values for a low-Reynolds-number turbulent boundary layer[44]. The distribution of the skin friction coefficient in the symmetry plane fairly matches the trend of the shape factor: the curve departs from the Blasius solution $C_f = 0.664/\sqrt{Re_x}$, and ultimately oscillates around the turbulent correlation curve.

Figure 10(a) shows the distribution along the entire $x-z$ plane of the skin friction coefficient. The near-field distribution of the skin friction coefficient well resembles the one found by Zhou and
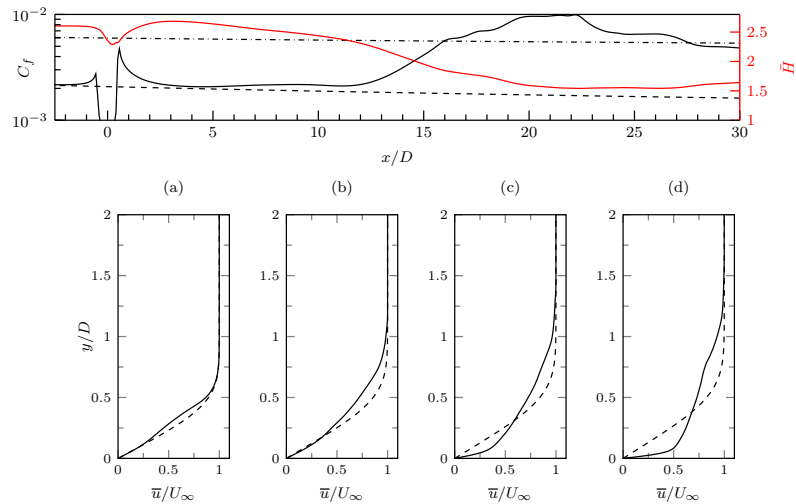
18

FIG. 9. (top) Streamwise distribution of the time-averaged skin friction coefficient C_f in the symmetry plane (solid black line) and the time-averaged boundary layer shape factor (red line). Laminar solution (Blasius curve, dashed line) and the turbulent correlation (dot-dashed line) are shown for the skin friction coefficient. (bottom) Wall-normal distributions of time-average streamwise velocity at four streamwise stations: (a) $x/D = 3$; (b) $x/D = 12$; (c) $x/D = 16$; (d) $x/D = 20$; controlled case (solid line), uncontrolled solution (dashed line). Case S1.

Zhang[6] for the laminar case, consisting in two legs of higher friction (corresponding to the motion of the hairpin legs) starting from the orifice lips, and spreading while moving downstream. A region of intense shear appears along the symmetry plane for $x/D \geq 15$; this feature is consistent with the near-wall vortical structures identified in figure 6, and corresponds to the onset of the transition region.

A useful metric to quantitatively detect the transition onset is given by the streamwise distribution of spanwise-averaged skin friction. Two different curves are reported for this quantity in Figure 10(b), namely $C_{f,avg}$ and $C'_{f,avg}$. The former quantity is averaged only inside the wedge shown in Figure 7, $|z| < l_z(x)$ (previously obtained by the u_{rms} distribution in figure 7), the latter along the entire z width. The figure reveals that $C'_{f,avg}$ monotonically increases along the streamwise direction, differently from the friction symmetry-plane distribution and the spanwise-average

19
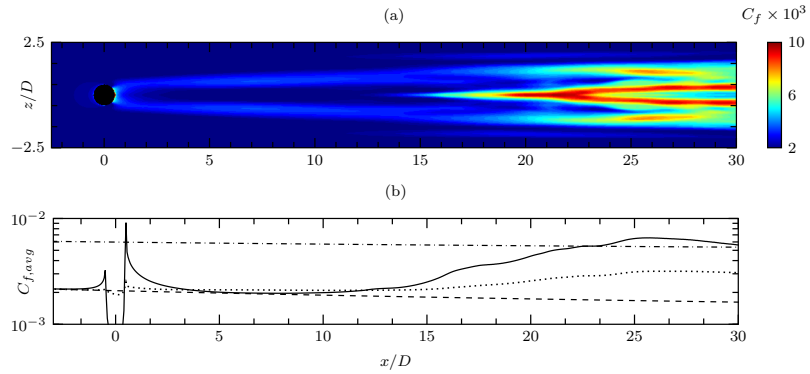
FIG. 10. (a) Contour plot of the time-averaged skin friction coefficient C_f in the $x - z$ plane; (b) streamwise distribution of the spanwise-averaged skin friction coefficients $C_{f,avg}$ (solid curve) and $C'_{f,avg}$ (dotted curve); comparison with the laminar solution (Blasius curve, dashed line) and the turbulent correlation (dot-dashed line), case S1.

inside the perturbed region only. The increasing behaviour of $C'_{f,avg}$ is obviously caused by the increasing C_f trend along each $z = const$ slice, but also due to the jet spreading, which increases its spanwise extension while moving downstream. However, $C'_{f,avg}$ never meets the turbulent correlation, as an external laminar region still exists even for large x values; for this reason $C_{f,avg}$ will be considered in the subsequent analysis to analyze turbulent transition, as its distribution depends only on the friction generated inside the turbulent region.

IV. PARAMETRIC ANALYSIS

The effects of the main SJ operation parameters and free stream turbulence are discussed separately in the present section.

A. Effect of reduced frequency

Figure 11 depicts the evolution of the vortex structures in the streamwise direction for cases S2 and S3. Whereas flow topologies are similar for all cases, it is apparent that vortex spreading increases with F^+, as reported in table II for $x/D = 30$. On the other hand, the streamwise distance

20

between two consecutive hairpin structures is smaller. The latter feature is consistent with the choice of the actuation frequency, as the hairpin spacing is monotonically decreasing with this quantity. As regards Cases S5 ans S6, the interaction of the jet with the boundary layer is rather weak, and no vortical structures are detected past the jet exit.
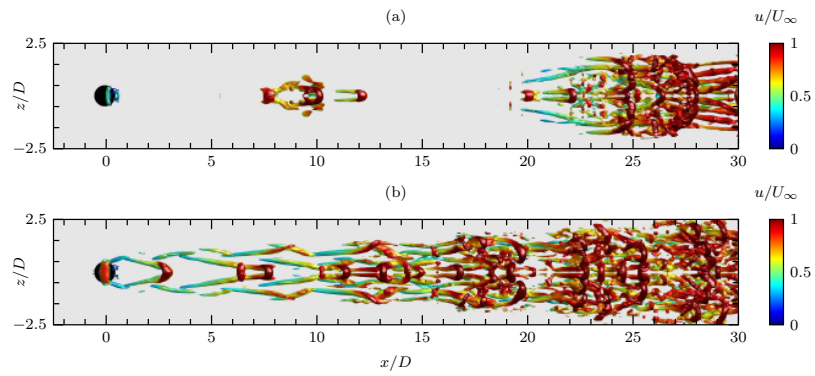
FIG. 11. Streamwise evolution of the vortical structures arising from the jet-boundary layer interaction: isosurfaces of $\lambda_2 = -0.025$ coloured by values of the instantaneous streamwise velocity component. $t/T = 10$, (a) $F_j^+ = 0.5$, (b) $F_j^+ = 2$.

The distributions of the diagnostic functions described in section III C are shown in figure 12. The strongest departure from the laminar solution is observed for the S3 and S4 cases, as their skin friction distributions attain values close to the turbulent correlations even for $x/D \approx 10$. In addition, these cases are characterized by the largest streak amplitude; case S3, instead, has the largest perturbation energy across the entire domain. The control strategy is effective in obtaining early transition also for $F_j^+ = 0.5$, although the transition from the laminar solution is slower than in the previously analyzed cases.

A conventional definition of the transition region can be based on the departure of the spanwise-averaged skin friction coefficient $C_{f,avg}$ from the Blasius solution. In the present work the transition onset x_{tr} is defined as the streamwise location where, for the first time, $C_{f,avg} \geq (C_{f,lam} + C_{f,turb})/2$. This parameter allows to compare the effectiveness of the synthetic jet actuator in obtaining a fast transition to turbulence for different values of the operation parameters. Table II reports the behaviour of x_{tr}/D for all the synthetic jet actuation frequency F_j^+ under scrutiny: case
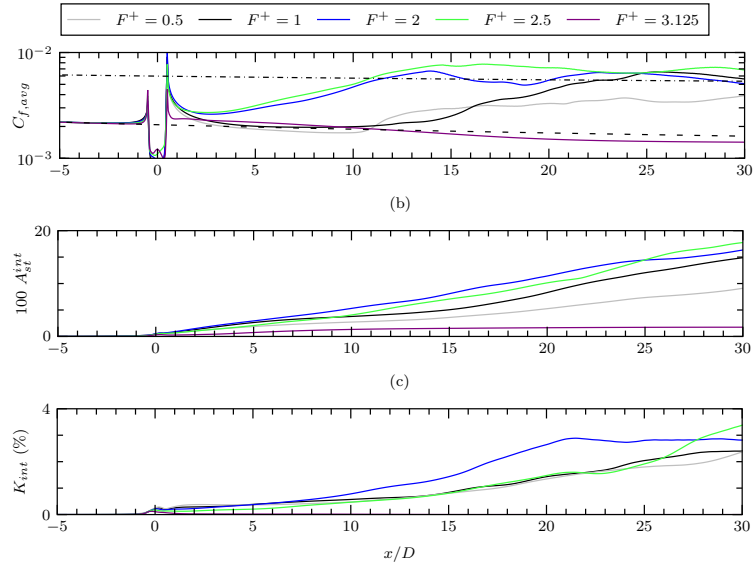
21

FIG. 12. Streamwise distribution of the time-averaged friction coefficient inside the turbulent region (a), streak amplitude (b) and integrated fluctuation energy (c). Colours are as in table I.

Case	F_j^+	x_{tr}/D	$l_{z,30}/D$
S2	0.5	23.0	1.2
S1	1.0	18.0	1.8
S3	2.0	8.7	2.4
S4	2.5	8.1	1.5
S5	3.125	x	x
S6	4	x	x

TABLE II. Transition onset, x_{tr}, and spanwise width at $x/D = 30$, $l_{z,30}/D$, as a function of the reduced operation frequency.

S4 is characterized by the earliest transition point ($x_{tr}/D \approx 8$), whereas case S2 has the largest x_{tr} value among all successful control cases. A decreasing trend of the transition point location is noted for $F_j^+ \leq 2.5$, and no transition is detected for $F_j^+ > 2.5$.

22
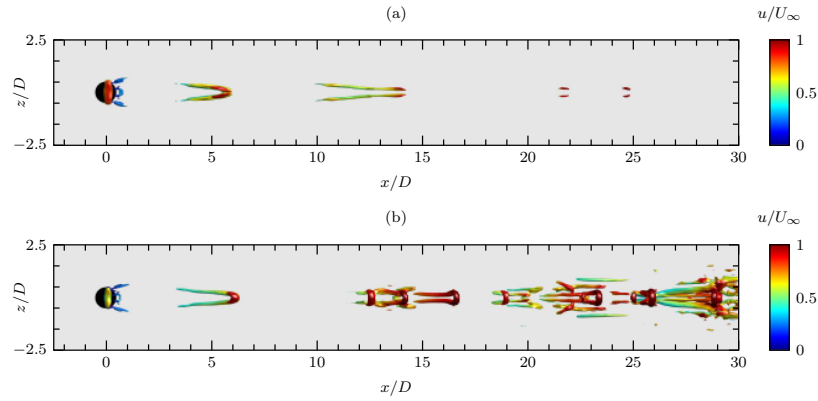
FIG. 13. Streamwise evolution of the vortical structures arising from the jet-boundary layer interaction: isosurfaces of $\lambda_2 = -0.01$ (a) or $\lambda_2 = -0.025$ (b) coloured by values of the instantaneous streamwise velocity component. $t/T = 10$, (a) Case S7, $C_\mu = 0.0026$, (b) Case S8, $C_\mu = 0.0059$.

As a result, it can be finally stated that SJ actuation is capable of modifying the boundary layer development on a flat plate, and the beginning of the transition region can be adjusted by changing the actuation frequency of the actuator. Cases S5-S6 show, however, that the control authority of the jet (in terms of achieving early transition) is not monotonically increasing with the actuation frequency, being optimal between cases S3 and S4 (among the investigated frequency range). In conclusion, the SJ effectiveness cannot be indefinitely improved by increasing the reduced frequency, as using high operation frequencies can be detrimental for the control strategy.

B. Effect of momentum coefficient

Figure 13 depicts the evolution of the vortex structures in the streamwise direction for cases S7 and S8. While case S8 shares the same topology of all the transitional cases shown above, case S7 is completely laminar. Indeed, the low momentum coefficient of the jet leads to the generation of weak vortical structures, which are barely visible even in the near field. Adjacent hairpin vortices never meet and completely dissipate themselves, without any possibility of tripping turbulent transition.

The diagnostic functions adopted in the previous sections, namely the integrated streak ampli-
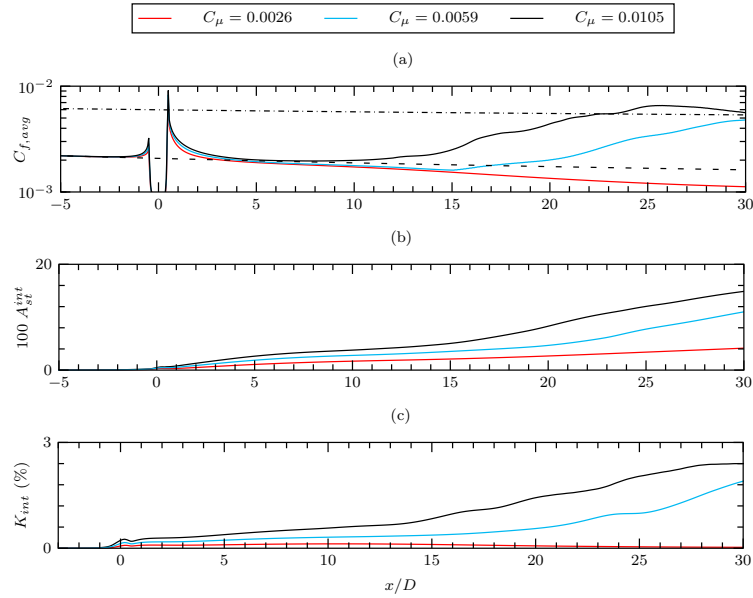
23

Physics of Fluids

FIG. 14. Streamwise distribution of the time-averaged friction coefficient inside the turbulent region (a), streak amplitude (b) and integrated fluctuation energy (c). Colours are as in table I.

tude, the skin friction coefficient and the integrated fluctuation energy, are reported in figure 14. It can be easily inferred that the impact of the synthetic jet on both time-average and fluctuation flow characteristics grows with C_μ. Indeed, case S7 never satisfies the condition $C_{f,avg} = (C_{f,l} + C_{f,t}/2)$ across the computational domain, whereas case S8 presents a delayed transition with respect to the reference, as reported in Table III. For this case, delayed spanwise growth of the transition wedge is also apparent, with $l_z(x/D = 30) \approx 1.2D$. The analysis of the time-average integral parameters reveals that Case S1 is also characterized by the largest values of A_{st}^{int} and K_{int} at every streamwise locations; it is noteworthy that both cases S1 and S8 present monotonic increase of A_{st}^{int} along the x direction, whereas the perturbation energy of case S7 peaks at $x/D \approx 10$ and then decays. The latter finding is consistent with the dissipation of the vortical structures observed in figure 13 (a).

Further insight on the behaviour of the streaky time-averaged solution can be obtained by analyzing the velocity deviation for cases S7 and S8, depicted in figure 15 (a-b). Case S7 clearly differs from the higher momentum controlled flows, being characterized by the presence of a

24

Case	C_μ	x_{tr}/D	$l_{z,30}/D$
S7	0.0026	x	x
S8	0.0059	25.8	1.2
S1	0.00105	18.0	1.8

TABLE III. Transition onset, x_{tr}, and spanwise width at $x/D = 30$, $l_{z,30}/D$, as a function of the operation momentum coefficient.
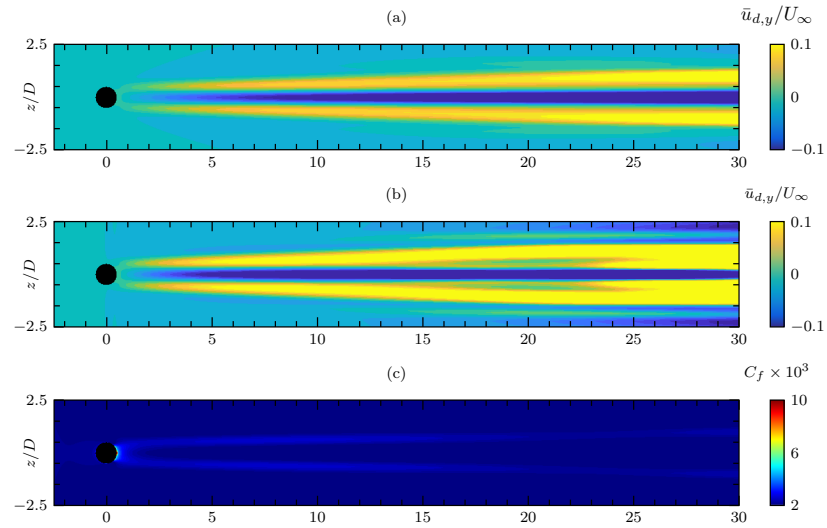

FIG. 15. (a-b) Contour plot of the velocity deviation $\bar{u}_{d,y}$ in the $x-z$ plane; (a) $C_\mu = 0.0026$, (b) $C_\mu = 0.0059$. (c) Contour plot of the skin friction coefficient C_f in the $x-z$ plane, $C_\mu = 0.0026$.

spanwise minimum in the central region past the jet exit, and two symmetric maxima far from the symmetry plane. This behaviour can be attributed to a near-wall flow deceleration behind the jet, which results in reduced skin friction coefficient in that area, and a corresponding flow acceleration towards the external region, as demonstrated also in figure 15 (c).

25
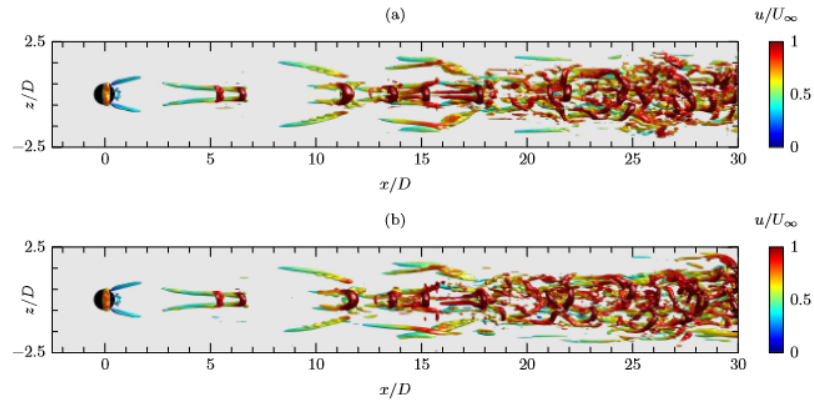
FIG. 16. Streamwise evolution of the vortical structures arising from the jet-boundary layer interaction: isosurfaces of $\lambda_2 = -0.025$ coloured by values of the instantaneous streamwise velocity component. $t/T = 10$, (a) Case S9 ($Tu_\infty = 2\%$), (b) Case S10 ($Tu_\infty = 4\%$).

C. Receptivity to freestream turbulence

An important feature of flow control devices is the robustness to perturbations of the inflow conditions. Two values of the inlet free stream turbulent intensity are considered, $Tu_\infty = 2\%$ and $Tu_\infty = 4\%$. Figure 16 depicts the evolution of the hairpin structures by means of isosurfaces of the λ_2 parameter, to monitor the effect of FST on the controlled flow field. It can be seen that in the near field the flow topology is practically identical to the reference. Conversely, the far-field behaviour is slightly modified by the turbulent perturbations, as symmetry-breaking motions appear. The vortex motion is characterized by the presence of asymmetric displacements of the vortical structures, which are more evident for high values of Tu_∞ and while moving along the streamwise direction. As a consequence, the flow reaches a chaotic state, which is more likely to be observed in practical applications.

Phase portraits and frequency spectra of the streamwise velocity in selected locations are shown in figure 17 for case S9: it can be seen that, different from the reference case, no peaks of the velocity spectra corresponding to the actuation frequency can be detected in the far field (probe at $x/D = 30$, green line). Moreover, a more broadband spectra is found at the farthest locations, where the flow approaches a turbulent state. On the other hand, the phase portraits (c) and (d)
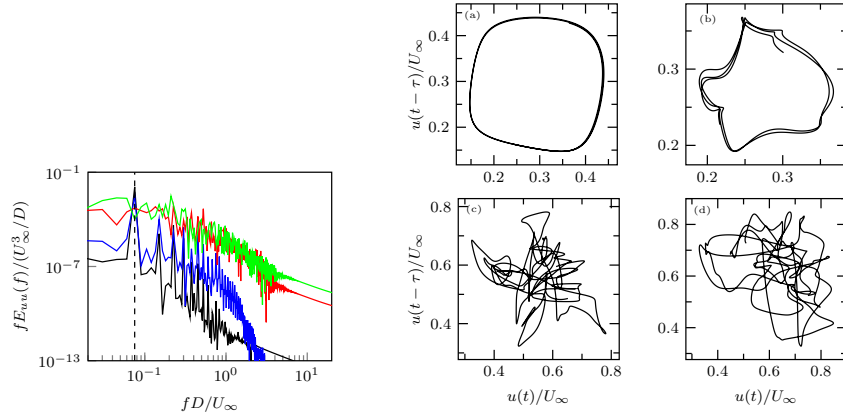
26

FIG. 17. (left) One-sided premultiplied frequency spectra of streamwise velocity component at different streamwise positions in the symmetry plane $(x/D, y/D)$: $(0, 0.125)$ (black line), $(10, 0.125)$ (blue line), $(20, 0.125)$ (red line), $(30, 0.125)$ (green line). The straight dashed line indicates the actuation frequency. (right) Phase portraits of streamwise velocity component, at $(x/D, y/D) = (0, 0.125)$ (a), $(x/D, y/D) = (10, 0.125)$ (b), $(x/D, y/D) = (20, 0.125)$ (c), $(x/D, y/D) = (30, 0.125)$ (d). Case S9 $(Tu_\infty = 2\%)$.

Case	Tu_∞	x_{tr}/D
S1	x	18.0
S9	2%	16.9
S10	4%	16.0

TABLE IV. Transition onset as a function of free stream turbulent intensity.

reveal that the velocity field does not follow the same trajectory in following cycles, as expected for a chaotic system.

Time-averaged skin friction coefficient distribution is of paramount importance in this context to assess the robustness of the control strategy to more general inlet perturbations. Figure 18 reveals that the spanwise-averaged friction coefficient is not significantly affected by FST, therefore the transition point is only anticipated slightly in presence of it. As a result, it can be stated that the transition process in the near-wall region is not dramatically affected by free stream turbulence, as reported by the summary in table IV.

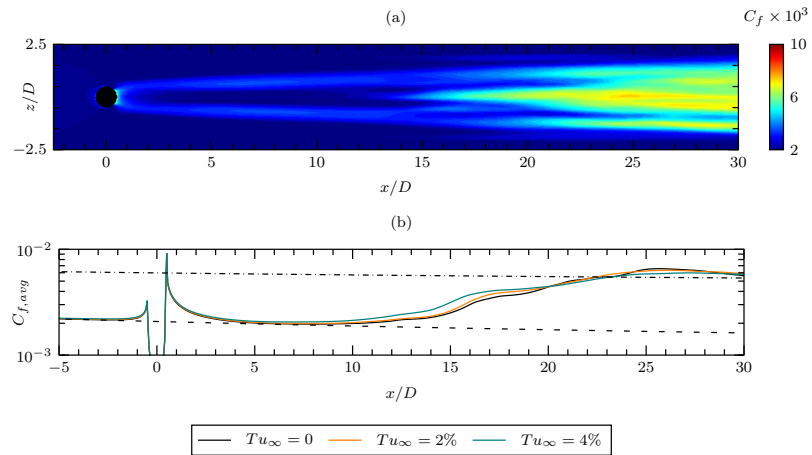Further evidence of the fulfilment of a turbulent flow condition is obtained by inspecting time-

FIG. 18. (a) Contour plot of the time-averaged skin friction coefficient C_f in the $x - z$ plane, case S9 ($Tu_\infty = 2\%$); (b) streamwise distribution of the spanwise-averaged skin friction coefficient $C_{f,z}$: laminar solution (Blasius curve, black dashed line) and the turbulent correlation (dot-dashed line) are also reported. Colours are as in table I.

average streamwise velocity and Reynolds stresses, collected past the transition point for case S10. In figure 19, blue curves represent wall-normal distributions of the time-averaged velocity and fluctuations at the transition location $x_{tr} = 16D$, black curves denote the end of the region of interest of the present study, $x/D = 30$, and red curves indicate profiles between such points. Wall-normal profiles in figure 19 are scaled by the local friction velocity $u_\tau = \sqrt{\tau_w/\rho}$, whereas the wall-normal coordinate is scaled with the local friction length $\delta_v = \nu/u_\tau$. As wall friction rises in $16 \leq x/D \leq 25$, the streamwise fluctuation peak move closer to the wall, in opposing behaviour with the transverse fluctuations. Clear overshoots of the velocity profiles and the fluctuation peaks are observed in the transition region. At the final streamwise location, the inner-scaled velocity profile $u^+ = \bar{u}/u_\tau$ appears to follow a quasi-logarithmic trend for $y^+ = y/\delta_v$ between 20 and 50, with smaller values than the usual log-law obtained for equilibrium turbulence. The overall behaviour of the curves presented in figure 19 is consistent with previous studies on bypass transition[45] and natural transition[46] of zero-pressure-gradient boundary layers, and streamwise velocity profiles at the most extreme streamwise location are in good agreement with experimental data of low-Reynolds number turbulent boundary layers[47].
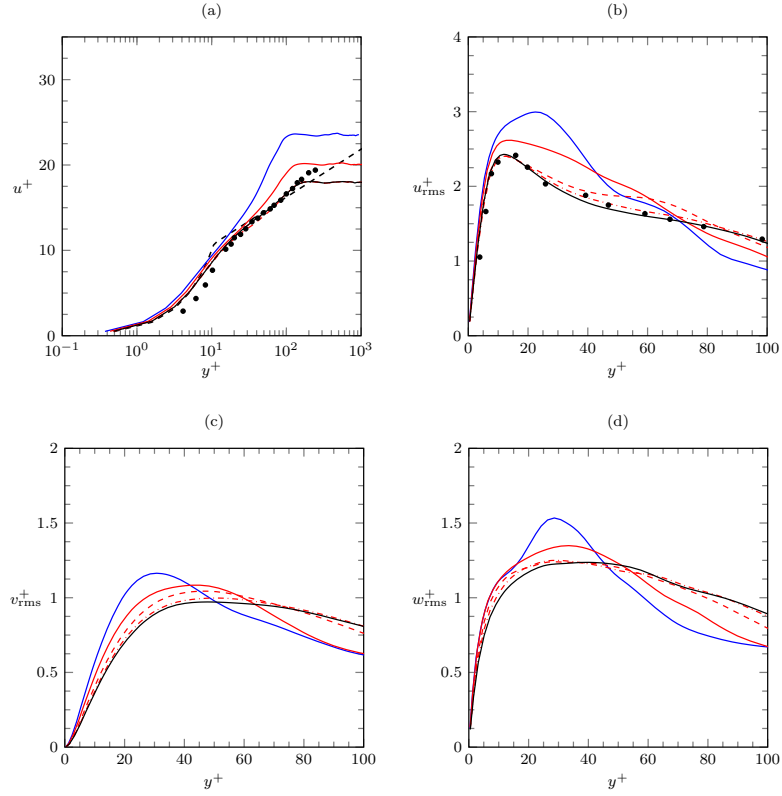
FIG. 19. Wall normal distributions of the inner-scaled time-averaged velocity $u^+ = \bar{u}/u_\tau$ (a) and velocity fluctuations u^+_{rms}, v^+_{rms}, w^+_{rms} (b-d) as a function of $y^+ = y/\delta_v$. Blue curves represent velocity profiles at $x/D = 16$, red curves denote profiles taken at $x/D = 20, 25, 28$; black curves are extracted at $x/D = 30$. The wall law $u^+ = \min(y^+, 1/0.41 \log(y^+) + 5)$ is depicted in panel (a) as a thick dashed line. Experimental data of streamwise time-averaged velocity and fluctuations (Purtell, Klebanoff, and Buckley [47], $Re_\theta = 465$) are represented by filled black circles in panels (a-b). Case S10 ($Tu_\infty = 4\%$).

V. SPECTRAL ANALYSIS AND MODAL DECOMPOSITION

Further insight on the phenomena associated with hairpin formation and turbulent transition of the controlled boundary layer can be gained by means of data-driven decomposition of the

flow. Finding the streamwise motion of the main vortical structures arising downstream of the jet exit plane and their eventual dissipation and breakup in smaller structures could better highlight the onset of the transition process for different values of the main non-dimensional parameters, thereby offering a complementary viewpoint to the time-averaged results shown in the previous sections.

The modal decomposition analyses presented in the present work relies on the Dynamic Mode Decomposition (DMD[48]), in conjunction with velocity spectra collected along the streamwise direction. DMD is applied on cases S1-S3-S4 to investigate the observed improvement of the control authority for F_j^+ ranging between 1 and 2.5. Cases S7-S8 are instead analyzed to clarify the effect of momentum coefficient. As for the previous analysis, the results of the analysis are first presented for the reference case (S1), while the effects of reduced frequency and momentum coefficient are discussed in the following sections.

The basic assumption of DMD relies on the possibility of decomposing a given dataset into a set of modes, each one with a single characteristic frequency and growth rate. The determination of both the modes and their characteristic frequency is based on approximating the relationship between consecutive snapshots with a linear operator.[48,49] For this reason, two matrices are defined from snapshot data $\{u(x,t_k)\}$, with $k = 0,...,N_s$:

$$X = [u(t_0)\, u(t_1)\, u(t_2)\, \ldots\, u(t_{s-1})],\tag{12}$$

$$X^{\#} = [u(t_1)\, u(t_2)\, u(t_3)\, \ldots\, u(t_s)].\tag{13}$$

A low-dimensional approximation of the DMD operator A is given by the following expression

$$U_r^T A U_r = U_r^T X^{\#} V_r \Sigma_r^{-1},\tag{14}$$

where $X = U_r \Sigma_r V_r^T$ is the truncated singular value decomposition of the snapshot matrix X and r the number of retained states. Once defined the low-dimensional operator $S = U_r^T A U_r$, which is a matrix of dimension $r \times r$, its eigenvalues and eigenvectors can be used to approximate a subset of the actual modes of the linear operator A. In particular, given the eigendecomposition $S = W \Lambda Z$, where $Z = W^{-1}$, the diagonal entries μ_i of Λ are referred to as Ritz values and constitute reasonable approximations of the eigenvalues of A, whereas the eigenvectors Φ of A can be obtained as

$$\Phi \approx U_r W.$$

The (complex) frequency of each DMD mode is obtained as $\lambda_i = \log(\mu_i)/(2\pi\Delta T_s)$, where ΔT_s is the sampling period. Finally, the decomposition of the k−th snapshot is computed as $u_k = S^k u_0$.

By exploiting previous S decomposition, the projection of the initial condition onto the $j-$th mode is $\alpha_j = z_j u_0$ (where z_j is a left eigenvector of S), and finally

$$u(x, t_k) = W\Lambda^k Z u_0 \approx \sum_{j=1}^{r} \alpha_j \mu_j^k w_j. \tag{15}$$

The DMD weights α_j constitute the contribution of each DMD mode to the initial condition, thus allowing proper ranking of each DMD mode.

Physical interpretation and main applications of the dynamic mode decomposition method can be gathered from the rich literature appeared on the subject in the last decade, as reported in recent review works[50,51]. In the present case, DMD is used to identify the mechanisms at work in the interaction between the SJ and the BL and the associated coherent structures. A previous work on the analysis of the transitional BL using DMD can be found in Sayadi *et al.*[52], where a reduced-order model of the late stages of H-type/K-type transition is developed. In this context, DMD allowed them to assess the contribution of the global frequencies of the flow to the Reynolds stress production. Similar to their study, the present work exploits DMD to investigate the development of the perturbation energy along the streamwise direction, and its distribution between the forcing frequency (which is expected to dominate on the other modes, at least in the near-field region) and higher frequency coherent structures, whose streamwise energy growth would be a strong evidence of the transition process.

A. Reference case

The DMD analysis has been carried out using a total number of 80 snapshots for case S1, extracted from the last 5 cycles of the simulation. Such a choice is dictated by the need of obtaining both the modes associated to the fundamental hairpin frequency (which is the actuation one) and the main harmonics; on the other hand, the relatively small number of snapshots is justified by the limit-cycle flow behaviour. The DMD spectrum and the DMD weights are shown in figure 20 (left) and (right), respectively: it is noteworthy that all the DMD modes are characterized by $|\mu_i| \leq 1$.

The DMD spectrum is composed by pairs of complex conjugate modes; their frequencies are multiples of the actuation one. It is observed that the highest perturbation energy is found for the DMD at the forcing frequency $F^+ = 1$. The amplitudes of the DMD modes at higher frequency monotonically diminish for increasing F^+. The description of the spectrum is completed by a set
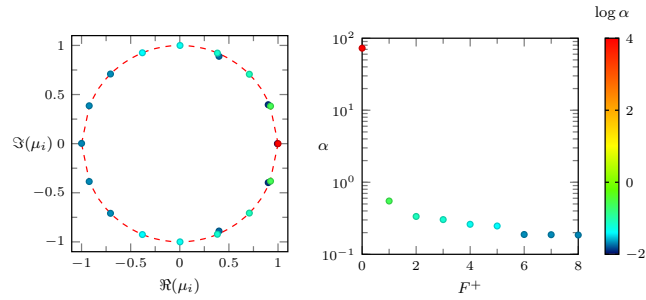
FIG. 20. DMD velocity spectrum (left) and associated weights of the modes with $|\mu_i| > 0.99$ (right). Reference case S1. In both figures, DMD modes are coloured according to their weight α.
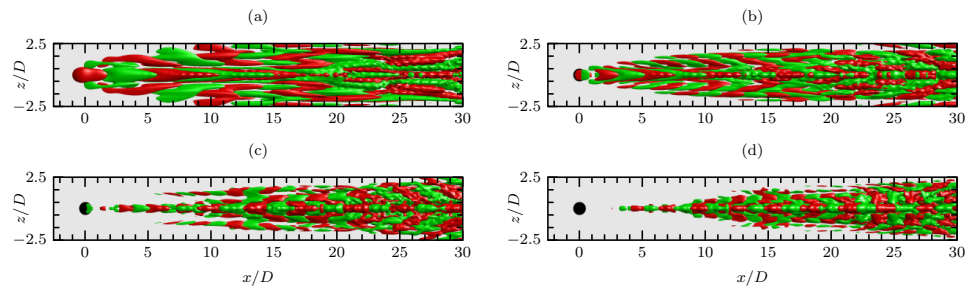

FIG. 21. Real part of the streamwise velocity perturbation u'_i of the leading DMD velocity modes: iso-surfaces of the streamwise velocity perturbation ($\pm 2.5\%$ of maximum velocity perturbation amplitude). $F^+ = 1$ (a), $F^+ = 2$ (b), $F^+ = 3$ (c), $F^+ = 4$ (d). Reference case S1.

of decaying eigenvalues, possibly depending on incomplete fulfillment of limit-cycle behaviour. These modes (not shown herein) are mainly clustered at the streamwise end of the domain and their amplitude is relatively weak.

The spatial shapes of the leading eigenmodes ($F^+ = 1, 2, 3, 4$) are reported in figure 21, in terms of their streamwise velocity: only varicose modes are retrieved from DMD, in accordance with instantaneous flow features in figure 3 . Each mode is characterized by own different streamwise and spanwise wavelengths, which are smaller for high-frequency modes. Whereas low-frequency modes exist across the entire streamwise extension of the domain, the high-frequency ones become relevant mainly in the transition region, being basically invisible at the jet exit.
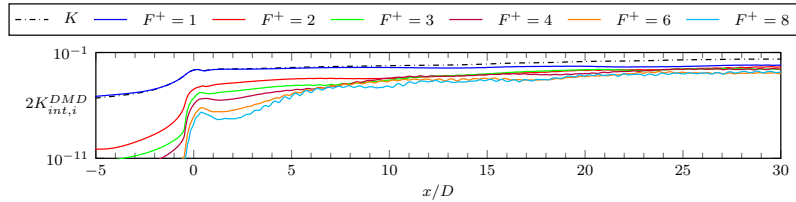
FIG. 22. Streamwise distribution of the integrated DMD fluctuation energy along the streamwise domain. The integrated fluctuation energy K is reported as a thin dash-dotted line. Note that each $K_{int,i}^{DMD}$ distribution is multiplied by 2 as DMD modes are organized in pairs. Reference case S1.

The relative importance of each mode at a fixed streamwise station on the total fluctuation energy can be inspected by means of the integrated DMD perturbation energy, defined as

$$K_{int,i}^{DMD}(x) = \frac{\alpha_i^2}{2U_\infty^2} \int_{-1/2}^{1/2} \int_0^{\eta^*} (u_i' u_i'^* + v_i' v_i'^* + w_i' w_i'^*) d\eta \, d\bar{z}, \tag{16}$$

which basically gives the fraction of the fluctuation energy at a certain x location carried by the i-th mode. In equation (16) u_i', v_i', w_i' are the velocity components of the i−th DMD mode and $(\cdot)^*$ is used for complex conjugation. As depicted in figure 22, the contribution of the leading mode $F^+ = 1$ overwhelms the others along the transition region, whereas all modes are relevant for $x/D > 20$. This finding is in good agreement with streamwise velocity spectra, collected at three different locations along the streamwise axis for a fixed height ($y \approx \delta_0^*/2$), shown in Fig. 23. Indeed, at the jet exit station the peak associated with $F^+ = 1$ is at least one order of magnitude bigger than the others; differently, all peaks have similar importance at $x/D = 30$.

B. Effect of reduced frequency

The effect of the reduced frequency F_j^+ on the streamwise development of the perturbation energy is investigated in figure 24. As for the reference case S1, also for cases S3 and S4 the largest DMD amplitudes are retrieved for the modes at the forcing frequency (which are denoted with filled symbols in figure 24). In particular, the DMD eigenvalue at the actuation frequency for case S3 has the largest amplitude among all modes. This finding is consistent with the fact that case S3 has the largest integrated perturbation energy K_{int}, as clearly shown in figure 12 (c).

Figure 25 reports the streamwise distributions of the previously defined DMD modal energy. As for the instantaneous flow motions represented in section IV A, all modes are characterized by
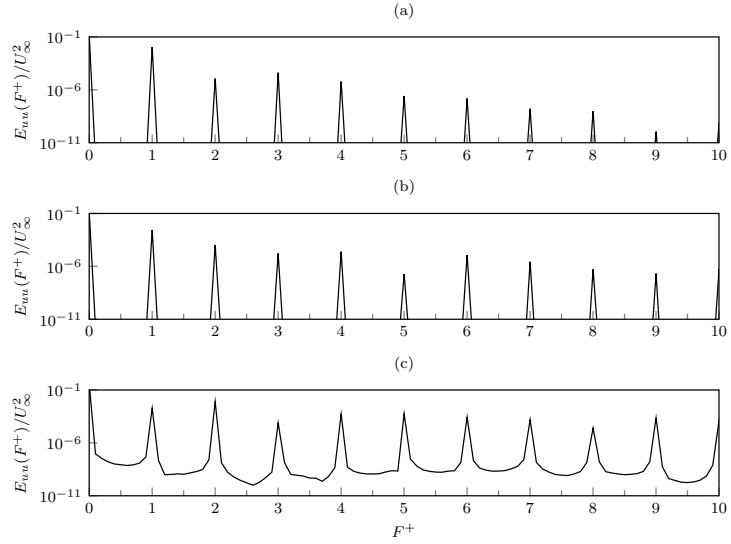
33

FIG. 23. Streamwise velocity frequency spectra at different streamwise positions along the symmetry plane $(x/D, y/D)$: from top to bottom (a) $(0, 0.125)$,(b) $(10, 0.125)$,(c) $(30, 0.125)$. Reference case S1.
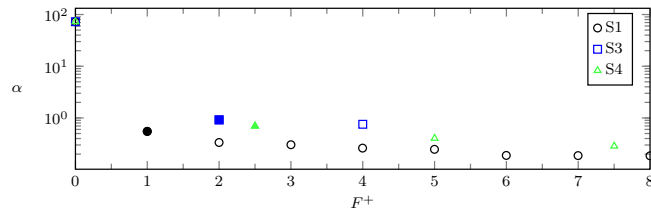

FIG. 24. DMD weights of the modes with $|\mu_i| > 0.99$. Reference case S1 (black circles); case S3 (blue squares); case S4 (green triangles). DMD weights associated to the actuation frequency are represented with filled symbols.

a varicose structure. The largest structures (in terms of streamwise wavelength) are observed for case S1, which is also characterized by the largest spanwise width for small x/D; however, all modes have roughly the same width at $x/D = 30$. This fact can be explained by the delayed spread of the flow for Cases S3 and S4: in particular, a closer look to figure 26 (c) reveals that the leading mode of Case S4 starts spreading only for $x/D \geq 15$, in contrast to the leading modes of Cases S1

34
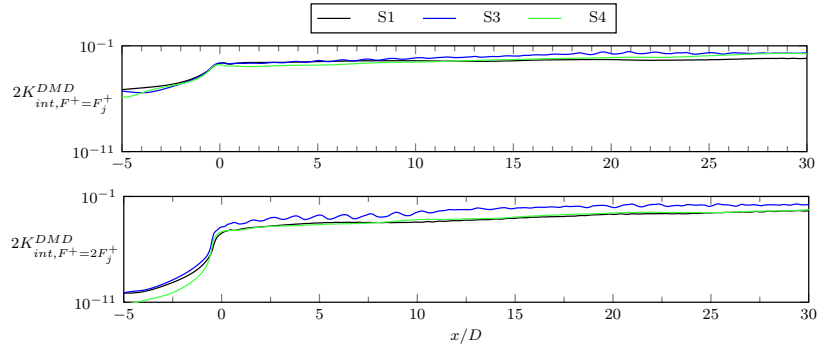
FIG. 25. Streamwise distribution of the integrated DMD fluctuation energy. (top) DMD mode associated to actuation frequency $F^+ = F_j^+$; (bottom) DMD mode at $F^+ = 2F_j^+$. Colours are as in table I.
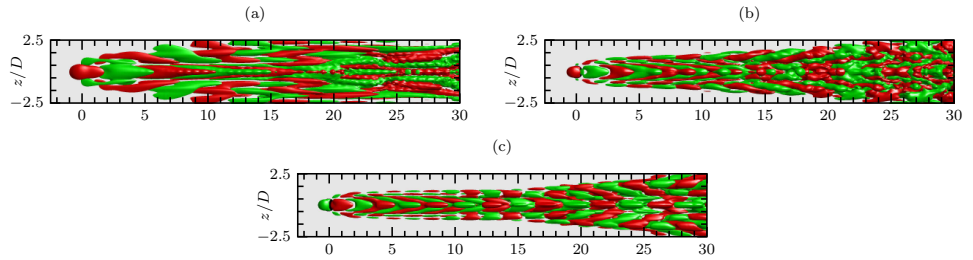

FIG. 26. Real part of the streamwise velocity perturbation u_i' of the leading DMD mode for cases S1 (a), S3 (b) and S4 (c): isosurfaces of the streamwise velocity perturbation ($\pm 2.5\%$ of maximum velocity perturbation amplitude).

and S3.

The distributions of the perturbation energy can shed light on the different transition behaviour as F_j^+ is changed. Case S3 is characterized by the largest values of K_{int}^{DMD} along the entire domain, both for the leading mode and the first harmonic. As the leading modes of Cases S1 and S3 have roughly the same integrated energy at $x/D = 0$, this means that for $F_j^+ = 2$ the jet perturbation is best amplified along its motion. Again, this fact explains why Case S3 is characterized by largest integrated perturbation energy K_{int} and earliest transition onset among all cases under scrutiny.
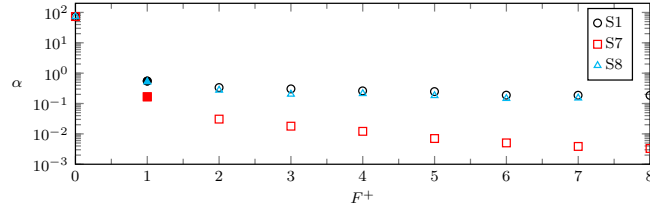
35

FIG. 27. DMD weights of the modes with $|\mu_i| > 0.99$. Reference case S1 (black circles); case S7 (red squares); case S8 (light blue triangles). DMD weights associated to the actuation frequency are represented with filled symbols.

C. Effect of momentum coefficient

The effect of the momentum coefficient C_μ on the controlled flow field is clearly outlined by figure 27, which reports the DMD weights for cases S1, S7, S8. Cases S1 and S8 share the same α_i distributions, with minor differences depending on the amount of perturbation energy initially imparted by the synthetic jet. On the contrary, the case S7 is characterized by strong reduction in the DMD weights, with high-frequency modes basically irrelevant with respect to the main one.

The different behaviour of these cases can be explained by analyzing the streamwise distributions of the perturbation energy at each frequency, reported in figure 28. The perturbation energy of the leading mode ($F^+ = 1$) for case S7 initially increases, then peaks at $x/D \approx 10$ and eventually decreases to smaller values. Similar trends can be found for the high-frequency modes, with different values of the streamwise peak ($x/D \approx 7$ and $x/D \approx 20$ for $F^+ = 2$ and $F^+ = 4$). Again, this fact suggest the existence of a critical value of C_μ between 0.0026 and 0.0059 for successful tripping.

The decreasing behaviour of the perturbation energy is consistent with the streamwise velocity spectra in figure 29, which shows monotonic decrease of the velocity spectra along the streamwise domain for all frequencies. The velocity spectra collected at the farthest locations are still composed of several peaks (corresponding to the actuation frequency and its multiples), but their intensity decays while moving downstream, and no energy is associated to higher frequencies. These findings give evidence of both the laminar nature of the flow throughout the entire domain and the dissipation of the hairpin vortices in the streamwise direction.
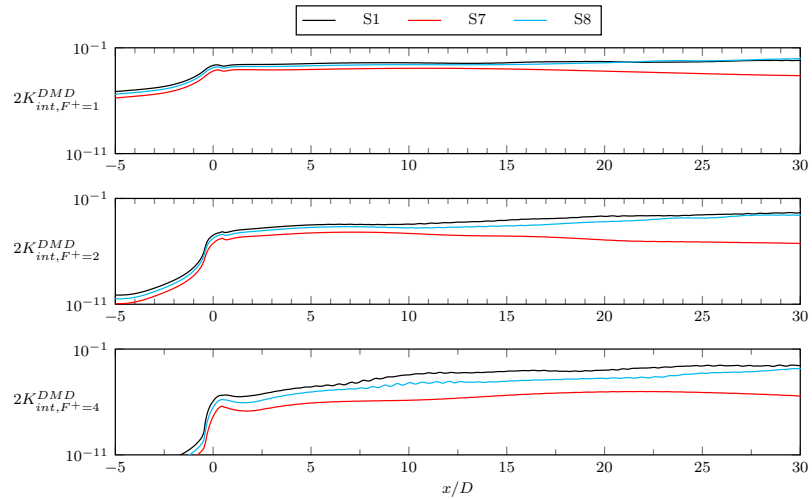
FIG. 28. Streamwise distribution of the integrated DMD fluctuation energy. From top to bottom: DMD modes at $F^+ = F_j^+ = 1$; $F^+ = 2$; $F^+ = 4$. Colours are as in table I.

VI. DISCUSSION AND CONCLUDING REMARKS

The effect of a low-speed synthetic jet on the transitional development of a laminar boundary layer is investigated using direct numerical simulations of the controlled flow field. The influence of the main non-dimensional parameters, namely the momentum coefficient and the reduced frequency is analyzed. The considered range of variation for F^+ includes both the temporal frequency of the most spatially amplified TS wave and the characteristic frequency of a low-speed continuous jet in crossflow at the same boundary layer conditions. As clearly demonstrated by the present study, neither phenomena play any role on the bypass transition induced by the jet/BL interaction. Notably, the reduced frequency which allows fastest flow transition falls within these two reference frequencies.

Skin friction coefficient distributions are compared to analyze the transition onset, while the strength of the time-averaged streaky structures generated at the SJ orifice is investigated to shed light on the mean flow departure from the uncontrolled flow. It is important to note that the high-fidelity simulations proposed in the present work are the only way to reliably estimate the transitional flow behaviour, whereas other computational solutions would fail in predicting the
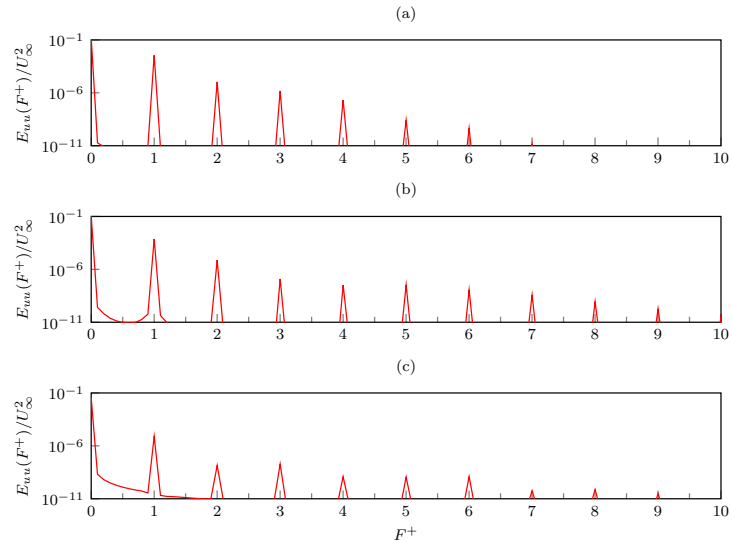
37

FIG. 29. Streamwise velocity frequency spectra at different streamwise positions along the symmetry plane $(x/D, y/D)$: from top to bottom (a) $(0, 0.125)$,(b) $(10, 0.125)$,(c) $(30, 0.125)$. Case S7 ($C_\mu = 0.0026$).

correct transition onset and perturbation energy growth. In this respect, the present results can be used to calibrate simpler numerical models, not based on DNS, with reduced computational cost. Finally, flow unsteadiness is analyzed by means of the definition of an integrated perturbation amplitude first, and then by means of DMD and velocity spectra.

A first result of the analysis is the striking similarity between the present case and the boundary layer transition induced by passive roughness elements. The flow field topology generated by the jet-boundary layer interaction for successful control cases fairly resembles the unsteady flow field downstream of an isolated cylindrical roughness immersed in a boundary layer flow. Likewise, the time-averaged flow topology is similar to the ones generated by other passive tripping devices, which are generally dominated by a streaky structure. Of course, the strength and the number of the vortical structures leading to turbulent transition are found to be strongly dependent on the momentum coefficient and the reduced frequency. In particular, it is found that forcing the boundary layer at the Tollmien-Schlichting frequency is not the optimal choice to obtain the fastest transition route (although it constitutes a decent frequency scale for the present analysis). In fact,

for the low-speed synthetic jets analyzed in the present work, using $F^+ = 2 - 2.5$ would be the best choice at this aim. Interestingly, these F^+ values are also below the typical frequency range of the global instability of a continuous jet in crossflow[53], meaning that neither TS frequency nor this flow conditions are suitable for synthetic jet actuation.

Synthetic jet actuators can be a flexible and robust way to trip transition, in contrast with passive devices. In fact, SJ actuators are found to be fairly robust to inlet perturbations, as shown in section IV C, in contrast with roughness elements, which reveal a relatively wide range of flow phenomena as the flow parameters are changed[29]. Moreover, as reported in figure 9, SJ-induced transition does not feature any wake region, which may trigger nonlinear coupling with external disturbances leading to control drawback[54]. The vortical structures generated by SJ actuators are basically produced by the ingestion/expulsion of flow from the orifice, rather than by global instability phenomena.

However, the most important aspect of the present parametric study is the definition of streamwise and spanwise lengthscales required for flow transition. As reported in the Introduction section, a common choice for the application of turbulators in low-Reynolds number flows is to place them sufficiently upstream of the separation region to be weakened/suppressed. In this respect, evaluating the streamwise location of transition is of utmost importance, but no information on this topic can be found in previous literature. The present analysis allows to state that the SJs are able to create a turbulent wedge, whose spanwise half-width exceeds $2D$ for $x/D = 30$ for $F^+ = 2$, and in which the time-averaged C_f meets the turbulent correlation curve in equation (11) about $10D$ past the jet exit. These results constitute valuable information for the design of a SJ array, as they also give an 'ideal' spanwise spacing between adjacent jets, depending also on the momentum coefficient.

Besides, concerning the design of the actuator geometry, once both C_μ and F^+ are chosen, lumped element models[9] can be used to target those values. It is noteworthy that the present work is intended to be coupled with a lumped approach for actuator design (indeed, the actuator cavity is not included with the computational setup), with the present simulations focusing only on the external flow field, and the latter method used to investigate the role of the actuator geometry on fixing the correct operation parameters.

Dynamic mode decomposition is also relevant to discuss the mechanisms leading to flow transition as the operation parameters are changed. In the near field, in all cases fluctuation energy is basically transported by the mode at the forcing frequency, with all the other modes being much

39

less important. However, in the transition region all modes share similar amplitude, as also outlined by the velocity Fourier spectra collected along the streamwise direction. This scenario is not followed by the lowest C_μ case, in which the DMD analysis reveals that all modes initially grow in energy and then decay due to viscous dissipation (with different peak positions, depending on the mode frequency).

In principle, the present DMD results can also provide an initial basis for more complex investigations not included in the present work, based on stability analysis. Resolvent analysis and/or pseudospectra of the linearized flow operator can be used to theoretically sustain the present results. Full stability studies of the jet/boundary layer interaction, based on Floquet analyses, can be also carried out to investigate possible bifurcations which, on account of previous literature, are apparent for high momentum coefficients[6]. It is worthwhile remarking that the latter analyses require huge computational effort; as a consequence the present results can be used to define a parameter space narrower than the one considered in the present work.

In conclusion, the present analysis shows that low-speed SJ actuators can be used as a reliable technique to fixate the location of the transition onset on a lifting surface, which is of crucial importance for all those industrial applications in which early transition is desired. More importantly, using low-speed jets can be beneficial for green technologies, as this operation regime allows low energy consumption. The present analysis provides an important backbone for more complex analyses on separated boundary layers and/or more complex shapes of the lifting surface. The definition of the typical transition location and the spanwise growth of the turbulent wedge generated by the jet can be used to optimally design SJ arrays.
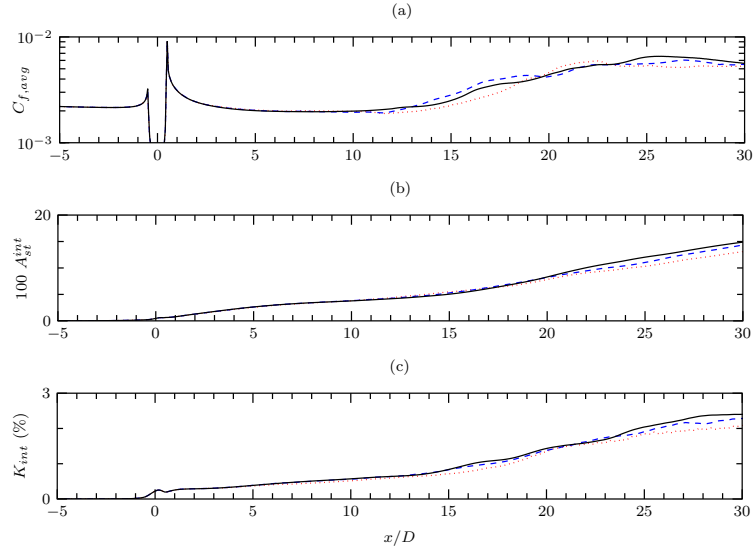
ACKNOWLEDGMENTS

FIG. 30. Domain dependence analysis: streamwise distribution of the time-averaged friction coefficient inside the turbulent region (a), streak amplitude (b) and integrated fluctuation energy (c). $N = 5$ (red dotted lines), $N = 7$ (blue dashed lines), $N = 9$ (black solid lines). Reference case S1.

Appendix A: Assessment of the numerical setup

The choices of the numerical domain and mesh distribution is made using several preliminary computations. A mesh independence analysis is performed using a $p-$grid convergence analysis, namely the polynomial order N of the spectral elements is gradually increased without changing the element distribution. Grid convergence is evaluated for the time-averaged quantities introduced in section III: the streak amplitude A_{st}^{int}, the spanwise-averaged skin friction coefficient $C_{f,avg}$ and the integrated fluctuation energy K_{int}. Figure 30 shows the results of the analysis, which involves three different polynomial orders: $N = \{5, 7, 9\}$. Negligible difference in the aforementioned quantities is found as the polynomial order is changed from 5 to 9. The transition point defined in section IV oscillates between $17 \leq x_{tr}/D \leq 18.5$ among the three grids under scrutiny. A summary of the grid convergence analysis is given in table V.

Another important step in the definition of the numerical setup is the choice of the inlet pipe

Case	N	$N_{\mathrm{dof}}/10^6$	x_{tr}/D
S1_N5	5	3.6	18.4
S1_N7	7	9.9	17.0
S1_N9	9	21.0	18.0

TABLE V. Summary of the grid independence study. The polynomial order N, the total number of degrees of freedom N_{dof} and the transition point location x_{tr} are reported.
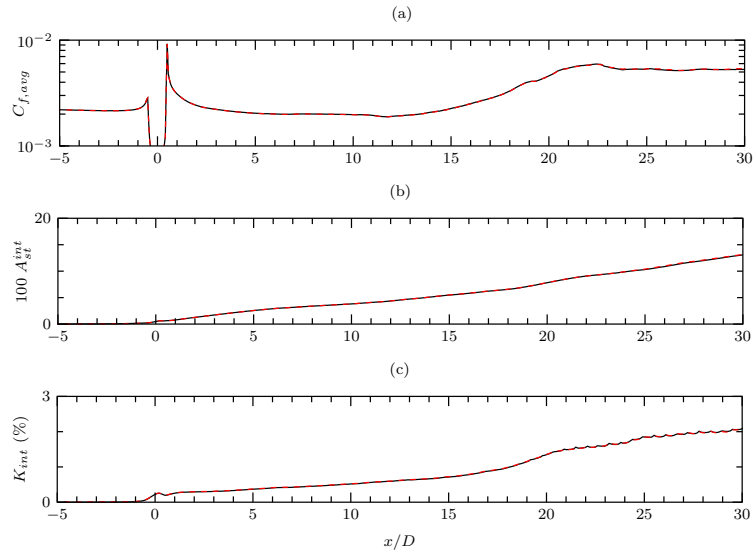

FIG. 31. Domain dependence analysis: time-averaged streamwise distributions of the time-averaged friction coefficient inside the turbulent region (a), streak amplitude (b) and integrated fluctuation energy (c). $H/D = 5$ (black solid lines), $H/D = 10$ (red dashed lines). Reference case S1, $N = 5$.

length, which could dramatically affect the flow behaviour. The possible influence of the H/D parameter is scrutinized by means of under-resolved simulations with polynomial order $N = 5$. Two simulations with $H/D = 5$ and $H/D = 10$ are performed: as demonstrated in figure 31, negligible difference on the metric functions is obtained by doubling the inlet pipe dimension, thus corroborating the validity of the present setup.

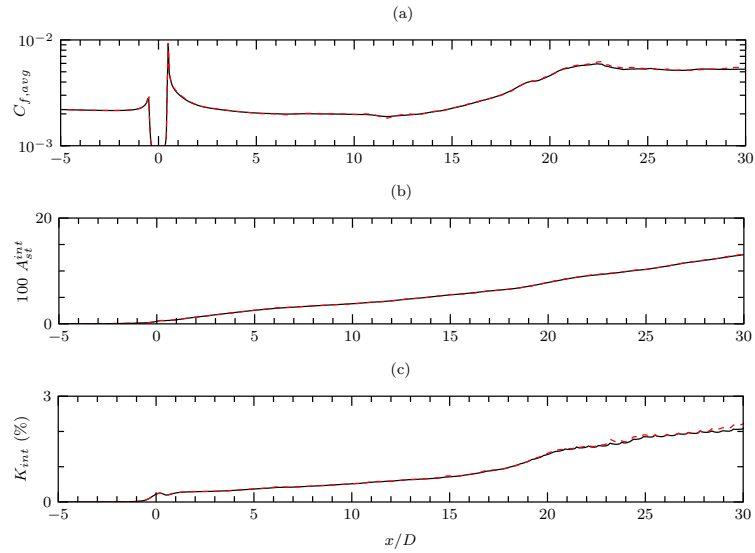Finally, the effect of the spanwise width of the numerical domain was examined. Two different

42

FIG. 32. Domain dependence analysis: time-averaged streamwise distributions of the time-averaged friction coefficient inside the turbulent region (a), streak amplitude (b) and integrated fluctuation energy (c). $L_z/D = 10$ (black solid lines), $L_z/D = 20$ (red dashed lines). Reference case S1, $N = 5$.

domains were tested, namely $L_z = \{10, 20\}D$, on the reference case S1. As clearly shown in figure 32, negligible difference in the streamwise distribution of the metric functions is found between the two computational domains. As a result, simulations with $L_z/D = 10$ can be considered as devoid of spurious effects due to periodicity, and this domain size is selected for the subsequent simulations.

Appendix B: Jet inlet boundary condition

As mentioned in section II, the Dirichlet boundary condition for the pulsating jet is given by equation (1), which has been originally obtained as the solution of a more general problem, a parallel flow within a pipe subject to a periodic pressure difference between its ends[43].

A preliminary computation of the inlet pipe only is carried out to ensure that the chosen inlet condition adequately models a fully-developed flow within an oscillating pipe. An axisymmetric

43

simulations of a cylindrical pipe (without any external environment) is performed: the flow is driven by a sinousoidally-varying plug inflow, whose amplitude V_{in} and frequency matches the inflow condition of the reference case (discussed in section III). The velocity on the free end of the cylindrical pipe is detected at different phases in order to validate the Womersley solution.

A sketch of the domain setup and boundary conditions is depicted in figure 33: the chosen pipe length is $L_p = 10D$, whereas the exit velocity profile is collected after the 20th cycle, which allows to obtain a periodic flow behaviour throughout the whole domain. An excellent agreement between the analytical solution and the numerical one is obtained, as highlighted in figure 34. This finding demonstrates that equation (1) can be used as a fully-developed pipe flow axial velocity profile to be used at the jet lower section ($y = -H$).
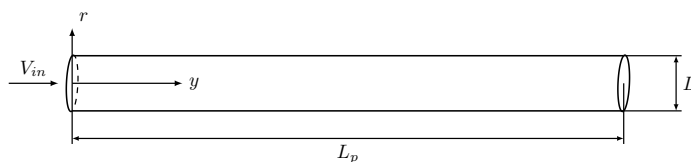

FIG. 33. Sketch of the numerical setup for the oscillating pipe flow validation case.
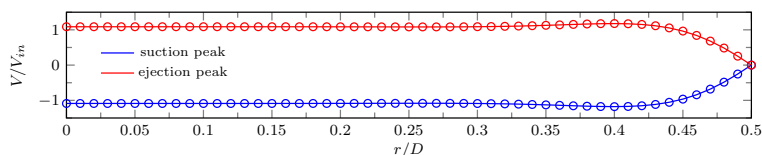

FIG. 34. Comparison between analytical (solid line) and numerical (open circles) results of the oscillating pipe flow. $Wo = 16.1$.

REFERENCES

[1]M. Gad-el Hak, *Flow Control: Passive, Active, and Reactive Flow Management* (Cambridge University Press, 2000).

[2]L. Cattafesta and M. Sheplak, "Actuators for active flow control," Annu. Rev. Fluid Mech. **43**, 247–272 (2010).

44

[3]P. Klebanoff and K. Tidstrom, "Mechanism by which a two-dimensional roughness element induces boundary-layer transition," Physics of Fluids **15**, 1173–1188 (1972).

[4]J. C. Lin, S. K. Robinson, R. J. McGhee, and W. O. Valarezo, "Separation control on high-lift airfoils via micro-vortex generators," Journal of aircraft **31**, 1317–1323 (1994).

[5]A. Glezer and M. Amitay, "Synthetic jets," Annu. Rev. Fluid Mech. **34**, 503–529 (2002).

[6]J. Zhou and S. Zhong, "Coherent structures produced by the interaction between synthetic jets and a laminar boundary layer and their surface shear stress patterns," Computers & Fluids **39**, 1296–1313 (2010).

[7]T. Van Buren, C. Leong, and E. Whalen, "Impact of orifice orientation on a finite-span synthetic jet interaction with a crossflow," Physics of Fluids **28**, (037106) 1–20 (2016).

[8]H. H. Ho, E. E. Essel, and P. E. Sullivan, "The interactions of a circular synthetic jet with a turbulent crossflow," Physics of Fluids **34**, 075108 (2022).

[9]M. Chiatto, A. Palumbo, and L. de Luca, "Design approach to predict synthetic jet formation and resonance amplifications," Experimental Thermal and Fluid Science **107**, 79–87 (2019).

[10]M. Amitay, A. Honohan, M. Trautman, and A. Glezer, "Modification of the aerodynamic characteristics of bluff bodies using fluidic actuators," in *28th Fluid Dynamics Conference* (1997) p. 2004.

[11]A. Crook, A. Sadri, and N. Wood, "The development and implementation of synthetic jets for the control of separated flow," in *17th Applied Aerodynamics Conference* (1999) p. 3176.

[12]J. Gilarranz, L. Traub, and O. Rediniotis, "A new class of synthetic jet actuators—part II: application to flow separation control," Journal of Fluids Engineering **127**, 377–387 (2005).

[13]K. Jansen, M. Rasquin, J. Farnsworth, N. Rathay, M. Monastero, and M. Amitay, "Interaction of a synthetic jet with separated flow over a vertical tail," AIAA Journal **56**, 2653–2668 (2018).

[14]M. Kim, E. Essel, and P. Sullivan, "Effect of varying frequency of a synthetic jet on flow separation over an airfoil," Physics of Fluids **34**, 015122 (2022).

[15]J. Dandois, E. Garnier, and P. Sagaut, "Numerical simulation of active separation control by a synthetic jet," Journal of Fluid Mechanics **574**, 25–58 (2007).

[16]G. Ceglia, M. Chiatto, C. S. Greco, F. De Gregorio, G. Cardone, and L. de Luca, "Active control of separated flow over 2D back-facing ramp by an array of finite-span slotted synthetic jets," Experimental Thermal and Fluid Science **129**, 110475 (2021).

[17]M. Amitay and A. Glezer, "Role of actuation frequency in controlled flow reattachment over a stalled airfoil," AIAA Journal **40**, 209–216 (2002).

45

[18]R. Mittal and P. Rampunggoon, "On the virtual aeroshaping effect of synthetic jets," Physics of Fluids **14**, 1533–1536 (2002).

[19]M. Jabbal and S. Zhong, "The near wall effect of synthetic jets in a boundary layer," International Journal of Heat and Fluid Flow **29**, 119–130 (2008).

[20]H. Zong and M. Kotsonis, "Effect of velocity ratio on the interaction between plasma synthetic jets and turbulent cross-flow," Journal of Fluid Mechanics **865**, 928–962 (2019).

[21]L. Wang and L.-H. Feng, "The interactions of rectangular synthetic jets with a laminar crossflow," Journal of Fluid Mechanics **899** (2020).

[22]D. Xiao, H. Borradaile, K.-S. Choi, L. Feng, J. Wang, and X. Mao, "Bypass transition in a boundary layer flow induced by plasma actuators," Journal of Fluid Mechanics **929** (2021).

[23]S. L. Brunton, B. R. Noack, and P. Koumoutsakos, "Machine learning for fluid mechanics," Annual Review of Fluid Mechanics **52**, 477–508 (2020).

[24]F. Capuano, A. Palumbo, and L. de Luca, "Comparative study of spectral-element and finite-volume solvers for direct numerical simulation of synthetic jets," Computers & Fluids **179**, 228–237 (2019).

[25]M. Bucci, D. Puckert, C. Andriano, J.-C. Loiseau, S. Cherubini, J.-C. Robinet, and U. Rist, "Roughness-induced transition by quasi-resonance of a varicose global mode," Journal of Fluid Mechanics **836**, 167–191 (2018).

[26]G. E. Karniadakis, M. Israeli, and S. A. Orszag, "High-order splitting methods for the incompressible navier-stokes equations," Journal of computational physics **97**, 414–443 (1991).

[27]Y. Maday, A. T. Patera, and E. M. Rønquist, "An operator-integration-factor splitting method for time-dependent problems: application to incompressible fluid flow," Journal of Scientific Computing **5**, 263–292 (1990).

[28]L. Brandt, P. Schlatter, and D. Henningson, "Transition in boundary layers subject to free-stream turbulence," Journal of Fluid Mechanics **517**, 167–198 (2004).

[29]M. A. Bucci, S. Cherubini, J.-C. Loiseau, and J.-C. Robinet, "Influence of freestream turbulence on the flow over a wall roughness," Physical Review Fluids **6**, 063903 (2021).

[30]R. Jacobs and P. Durbin, "Simulations of bypass transition," Journal of Fluid Mechanics **428**, 185 (2001).

[31]S. Shahinfar, *Transitional boundary layers caused by free-stream turbulence*, Ph.D. thesis, KTH Royal Institute of Technology (2011), *Available at http://urn.kb.se/resolve?urn=urn:nbn:se:kth:diva-34150*.

[32] J. H. Fransson and S. Shahinfar, "On the effect of free-stream turbulence on boundary-layer transition," Journal of Fluid Mechanics **899** (2020).

[33] B. Smith and A. Glezer, "The formation and the evolution of synthetic jets," Physics of Fluids **10**, 2281–2297 (1998).

[34] T. Berk, N. Hutchins, I. Marusic, and B. Ganapathisubramani, "Trajectory of a synthetic jet issuing into high-Reynolds-number turbulent boundary layers," Journal of Fluid Mechanics **856**, 531–551 (2018).

[35] J. E. Cater and J. Soria, "The evolution of round zero-net-mass-flux jets," Journal of Fluid Mechanics **472**, 167–200 (2002).

[36] K. Mohseni and R. Mittal, *Synthetic jets: fundamentals and applications* (CRC Press, 2014).

[37] J. Jeong and F. Hussain, "On the identification of a vortex," Journal of Fluid Mechanics **285**, 69–94 (1995).

[38] J. Kim and F. Hussain, "Propagation velocity of perturbations in turbulent channel flow," Physics of Fluids A: Fluid Dynamics **5**, 695–706 (1993).

[39] A. Fraser and H. Swinney, "Independent coordinates for strange attractors from mutual information," Physical Review A **33**, 1134 (1986).

[40] H. Kantz and T. Schreiber, *Nonlinear time series analysis*, Vol. 7 (Cambridge University Press, 2004).

[41] Q. Ye, F. F. Schrijer, and F. Scarano, "Boundary layer transition mechanisms behind a micro-ramp," Journal of Fluid Mechanics **793**, 132–161 (2016).

[42] L. Siconolfi, S. Camarri, and J. Fransson, "Stability analysis of boundary layers controlled by miniature vortex generators," Journal of Fluid Mechanics **784**, 596–618 (2015).

[43] F. White, *Viscous fluid flow*, Vol. 3 (McGraw-Hill New York, 2006).

[44] P. Schlatter and R. Örlü, "Assessment of direct numerical simulation data of turbulent boundary layers," Journal of Fluid Mechanics **659**, 116–126 (2010).

[45] X. Wu and P. Moin, "Direct numerical simulation of turbulence in a nominally zero-pressure-gradient flat-plate boundary layer," Journal of Fluid Mechanics **630**, 5–41 (2009).

[46] T. Sayadi, C. W. Hamman, and P. Moin, "Direct numerical simulation of complete H-type and K-type transitions with implications for the dynamics of turbulent boundary layers," Journal of Fluid Mechanics **724**, 480–509 (2013).

[47] L. Purtell, P. Klebanoff, and F. Buckley, "Turbulent boundary layer at low Reynolds number," The Physics of Fluids **24**, 802–811 (1981).

[48]P. J. Schmid, "Dynamic mode decomposition of numerical and experimental data," Journal of Fluid Mechanics **656**, 5–28 (2010).

[49]S. Bagheri, "Koopman-mode decomposition of the cylinder wake," Journal of Fluid Mechanics **726**, 596–623 (2013).

[50]J. N. Kutz, S. L. Brunton, B. W. Brunton, and J. L. Proctor, *Dynamic mode decomposition: data-driven modeling of complex systems* (SIAM, 2016).

[51]C. W. Rowley and S. T. Dawson, "Model reduction for flow analysis and control," Annu. Rev. Fluid Mech **49**, 387–417 (2017).

[52]T. Sayadi, P. J. Schmid, J. W. Nichols, and P. Moin, "Reduced-order representation of near-wall structures in the late transitional boundary layer," Journal of Fluid Mechanics **748**, 278–301 (2014).

[53]G. Chauvat, A. Peplinski, D. Henningson, and A. Hanifi, "Global linear analysis of a jet in cross-flow at low velocity ratios," Journal of Fluid Mechanics **889**, A12 (2020).

[54]D. K. Puckert and U. Rist, "Experimental observation of frequency lock-in of roughness-induced instabilities in a laminar boundary layer," Journal of Fluid Mechanics **870**, 680–697 (2019).